nature communications

Article

https://doi.org/10.1038/s41467-025-61141-1

Dimeric copper peptide incorporated hydrogel for promoting diabetic wound healing

Received: 9 January 2025

Accepted: 13 June 2025

Published online: 01 July 2025

Check for updates

Rui Cong[1,4], Chengyu Deng[1,4], Pengwei Li[1,4], Yiwei Tang[1], Jinfan Hou[1], Jiehui Zhao[1], Qili Wang[1], Yingying Chen[2], Jiasheng Tu[1] ✉, Xiqun Jiang[3] ✉ & Lei Jiang[1] ✉

Diabetic wounds require continuous and coordinated modulation of the microenvironment concurrent with tissue regeneration, which remains a significant challenge. As a proof of concept, we herein propose to use dimeric copper peptide (D-CuP) for diabetic wound treatment. The D-CuP is synthesized and then incorporated into a reactive oxygen species (ROS)-responsive hydrogel matrix to improve therapeutic compliance, culminating in the formulation of G/D-CuP. Compared to monomer copper peptide (M-CuP), a wound healing agent, D-CuP exhibits multivalency, enhanced biological stability against proteases, and broad biological activities. Meanwhile, the hydrogel matrix, exhibiting ROS-scavenging capabilities, has been engineered to be an intelligent drug reservoir for wound-responsive release of D-CuP at the wound site while simultaneously attenuating inflammatory responses. Ultimately, the G/D-CuP group demonstrates superior therapeutic efficacy, achieving 97.2% closure of infected wounds.

Dimerization is essential in biological systems, playing a key role in regulating physiological functions and regulatory mechanisms of living organisms[1,2]. This process involves the combination of two molecules or molecular fragments to form a higher-order structure via noncovalent interactions or covalent bonds, enabling the rapid construction of complex molecular architectures with diverse physiological properties[3,4]. In transcriptional regulation cascades, dimerization affects gene expression by modulating the activity of transcription factors[5,6]. It also contributes to the modulation of enzyme activity, which in turn impacts metabolic pathways and cellular processes[7,8]. Additionally, dimerization can stabilize proteins, helping them maintain their functional conformation and resist denaturation under physiological conditions as well as regulate intracellular signaling molecules[9,10]. Therefore, the formation of dimeric complexes is critical in preserving cellular balance and proper functions. Notably, dimerization presents opportunities for developing pharmaceuticals, especially those necessitating multiple target mechanisms and functions[11,12]. Dimeric compounds are promising for simultaneously targeting dual binding domains, enhancing molecular recognition precision and consequently optimizing reaction dynamics and biochemical selectivity[13,14]. When addressing dimeric protein targets, the ability of dimeric therapeutic agents to antagonize paired receptors within a single molecular entity potentially offers superior therapeutic efficacy and target selectivity[15,16].

Diabetic wounds are a prevalent type of chronic wound that significantly decreases patients' quality of life and imposes substantial clinical and economic burdens[17,18]. Studies indicate that in the absence of appropriate medical intervention, approximately 20% of patients with diabetic wounds will require lower limb amputation, with a subsequent one-year mortality rate of 13% post-diagnosis[19,20]. Key factors hindering the healing of diabetic wounds include persistent high level of reactive oxygen species (ROS), excessive inflammatory cells and cytokines in the wound microenvironment, insufficient new blood vessel formation, and weakened cell proliferation[21,22]. These elements

[1]State Key Laboratory of Natural Medicines, School of Pharmacy, China Pharmaceutical University, Nanjing, China. [2]Department of Materials Science and Engineering, University of Illinois at Urbana-Champaign, Urbana, IL, USA. [3]MOE Key Laboratory of High-Performance Polymer Materials and Technology and Department of Polymer Science & Engineering, College of Chemistry & Chemical Engineering, Nanjing University, Nanjing, China. [4]These authors contributed equally: Rui Cong, Chengyu Deng, Pengwei Li. ✉e-mail: jiashengtu@cpu.edu.cn; jiangx@nju.edu.cn; lei.jiang@cpu.edu.cn; jianglei0453@163.com

establish a feedback loop that delays tissue repair, making it essential to precisely regulate the localized microenvironment to address multiple pathogenic mechanisms simultaneously. Current wound management approaches focus on scavenging ROS[23,24], mitigating inflammation[25,26], modulating immunity[27,28], and enhancing tissue regeneration[29,30]. However, they are facing challenges in coordinating the individual components within the disordered diabetic wound microenvironment. Thus, designing an all-rounder with space-time ROS scavenging, modulation of macrophage polarization, and promotion of angiogenesis and cell proliferation is a prominent subject for advancing the clinical treatment of chronic diabetic wounds.

Many biologically active peptides, such as antimicrobial and antioxidant peptides, exhibit physiological functions and have the potential for tissue damage repair[31,32]. GHK (glycyl-l-histidyl-l-lysine) is an endogenous tripeptide isolated from plasma, which can coordinate with the organic cation Cu^{2+} to form a copper peptide (CuP) complex[33,34]. CuP demonstrates a wide range of biological activities, including antioxidative properties, inflammatory modulation, chemotactic cell recruitment, and promotion of angiogenesis and cell proliferation[35,36]. These properties make CuP therapeutically beneficial across all phases of wound healing. Nevertheless, CuP is prone to hydrolysis by proteases, resulting in treatment failure[34,37]. Techniques such as supramolecular self-assembly[38,39], macrocyclization[40,41], polymer conjugation[42,43] are commonly utilized to enhance the stability of bioactive peptides. However, in certain cases, they may interfere with the peptide's ability to interact with its target or disrupt bioactive conformation, significantly reducing its activity[44,45]. Additionally, these modifications may induce significant toxicity by triggering immune responses[46,47]. Consequently, there is an urgent need for innovative chemical structures and strategies to bolster the stability of bioactive peptides, while the production is convenient and cost-effective.

In this study, we present a proof-of-concept study to optimize the treatment of diabetic wounds (Fig. 1). This method integrates a dimeric copper peptide incorporated hydrogel (G/D-CuP) to address several critical factors: i) The design and synthesis of the dimeric copper peptide (D-CuP) feature a broad range of targets and enhanced biological activities, such as anti-inflammatory and antioxidative properties, while promoting angiogenesis and fibroblast proliferation and migration[33,48]; ii) Utilizing the steric hindrance conferred by dimerization reduces protease access to the active site and significantly improving stability against proteases[49,50]; iii) A ROS-responsive hydrogel matrix (G) has been synthesized, exhibiting superior ROS-scavenging capabilities, functioning as an intelligent drug reservoir that enables the controlled release of D-CuP at the wound interface while simultaneously attenuating inflammatory responses in the microenvironment[51]; iv) G/D-CuP possesses deformability and spreadability, allowing it to adapt to any wound shape; v) The synthesis and preparation process of G/D-CuP are straightforward and cost-effective, making it highly promising for clinical translation. This multifunctional treatment platform is anticipated to accommodate the complex and dynamic biological processes involved in diabetic wound healing, thereby significantly improving the overall efficacy of wound healing treatments.

Results

Preparation of the D-CuP

The dimeric peptide D-P was synthesized through the covalent conjugation of two glycyl-l-histidyl-l-lysine (GHK) tripeptide moieties utilizing lysine as the bridging molecule (Fig. 2a and Supplementary Fig. 1). The resulting product was characterized by ^{1}H NMR, ^{13}C NMR and HRMS (Supplementary Figs. 2–4), confirming successful synthesis. As shown in Fig. 2b, upon addition of $CuSO_4$ solution, a blue-purple D-CuP complex was formed in a molar ratio of GHK: Cu^{2+} = 1: 0.5. The UV-Vis absorption spectrum for D-CuP exhibited a distinct absorption peak at 584 nm, consistent with that of monomer copper peptide (M-CuP) (Fig. 2c). This result suggests the successful chelation of Cu^{2+} with D-P. When the molar ratio of the coordinating functional groups remains constant, the absorbance observed at 584 nm for the dimer was larger than that of the monomer peptide, indicating that D-P possesses better coordination efficacy and greater stability than M-P (Fig. 2d). Electron paramagnetic resonance (EPR) analysis further confirmed the formation of D-CuP through distinctive Cu^{2+} signals at ~3426 mT (Fig. 2e). The complex pathophysiology of wound microenvironments, characterized by fluctuating pH levels and elevated protease activity[52], necessitates a thorough assessment of the chemical stability of D-CuP. Under normal conditions, the skin exhibits a slightly acidic environment (pH 4–6) that helps sustain the epidermal barrier and inhibits bacterial intrusion. In contrast, during chronic or infected wound states, the pH shifts to alkaline levels (pH 7–9) as a result of microbial activity[53,54]. We evaluated the pH stability of D-CuP across the range of cutaneous wound conditions (pH 4–9). As illustrated in Supplementary Fig. 5, the characteristic absorption peak at 584 nm for both M-CuP and D-CuP exhibited no statistically significant variation across the tested pH range. This pH-adaptive stability spans both physiological skin acidity (pH 4–6) and the alkaline extremes (pH 7–9) typical for chronic wounds, confirming the ability of D-CuP to maintain structural integrity under pathological conditions. Protease K, a serine protease with broad cleavage activity, was employed to evaluate the protease stability of D-CuP in vitro. As shown in Fig. 2f, M-CuP degraded rapidly, retaining about 58% and 50% after 0.5 and 4 h, respectively. In contrast, approximately 92% and 87% of D-CuP remained unchanged after 0.5 and 4 h of protease K exposure, highlighting its superior protease stability. This may be attributed to the dimeric structure which hinders enzyme access to active sites, showcasing significant resistance to enzymatic degradation[49,55].

Preparation of the G/D-CuP

The overproduction of ROS can worsen tissue damage and inflammatory reactions, potentially delaying wound healing during the inflammation stage. Thus, eliminating surplus ROS is highly advantageous for wound healing[56,57]. The ROS-responsive linker (((ethane-1,2-diylbis(azanediyl))bis(carbonyl))bis(4,1-phenylene))diboronic acid (EBPBA) was synthesized (Supplementary Fig. 6), which can crosslink polyvinyl alcohol (PVA) to form a hydrogel with phenylboronic ester bonds and generate ROS responsiveness. The EBPBA structure was confirmed by ^{1}H NMR and ESI-MS (Supplementary Figs. 7, 8). Then, D-CuP loadedROS- responsive hydrogel was prepared and the preparation process was illustrated in Fig. 3a. G/D-CuP could quickly be formed by simply mixing PVA, EBPBA, and D-CuP solution. The hydrogel underwent crosslinking by the interaction of phenylboronic acids derived from EBPBA and hydroxyl groups from PVA, resulting in the formation of phenylboronic ester bonds. The rheology properties further confirmed that the hydrogel was successfully prepared. Scanning electron microscope (SEM) images revealed the 3D-network structure and pore structure of the G/D-CuP (Fig. 3b). As shown in Fig. 3c, under low strain conditions (0.1% to 1200%), G/D-CuP showed a storage modulus (G′) consistently surpassing the loss modulus (G″). This rheological behavior suggests that the hydrogel exhibits a semi-solid consistency with substantial elasticity, validating its successful formation. The frequency sweep results, as illustrated in Fig. 3d, indicated that the G′ of the G/D-CuP remained dominant over G″ across the tested range (0.1–500 rad·s^{-1}), confirming the establishment of a stable hydrogel network. The hydrogel, when covering wound surfaces, is susceptible to damage from skin movement, which could impede wound healing and increase infection risk. However, a self-healing hydrogel is capable of providing prolonged protection to wounds[58,59]. A continuous step strain test was conducted to evaluate the self-healing capacity of G/D-CuP. The G′ of G/D-CuP decreased from 2500 Pa (0.1% strain) to 390 Pa (1200% strain), but upon strain relief, the G′ recovered to 2500 Pa (Fig. 3e), indicating a temporary

https://doi.org/10.1038/s41467-025-61141-1

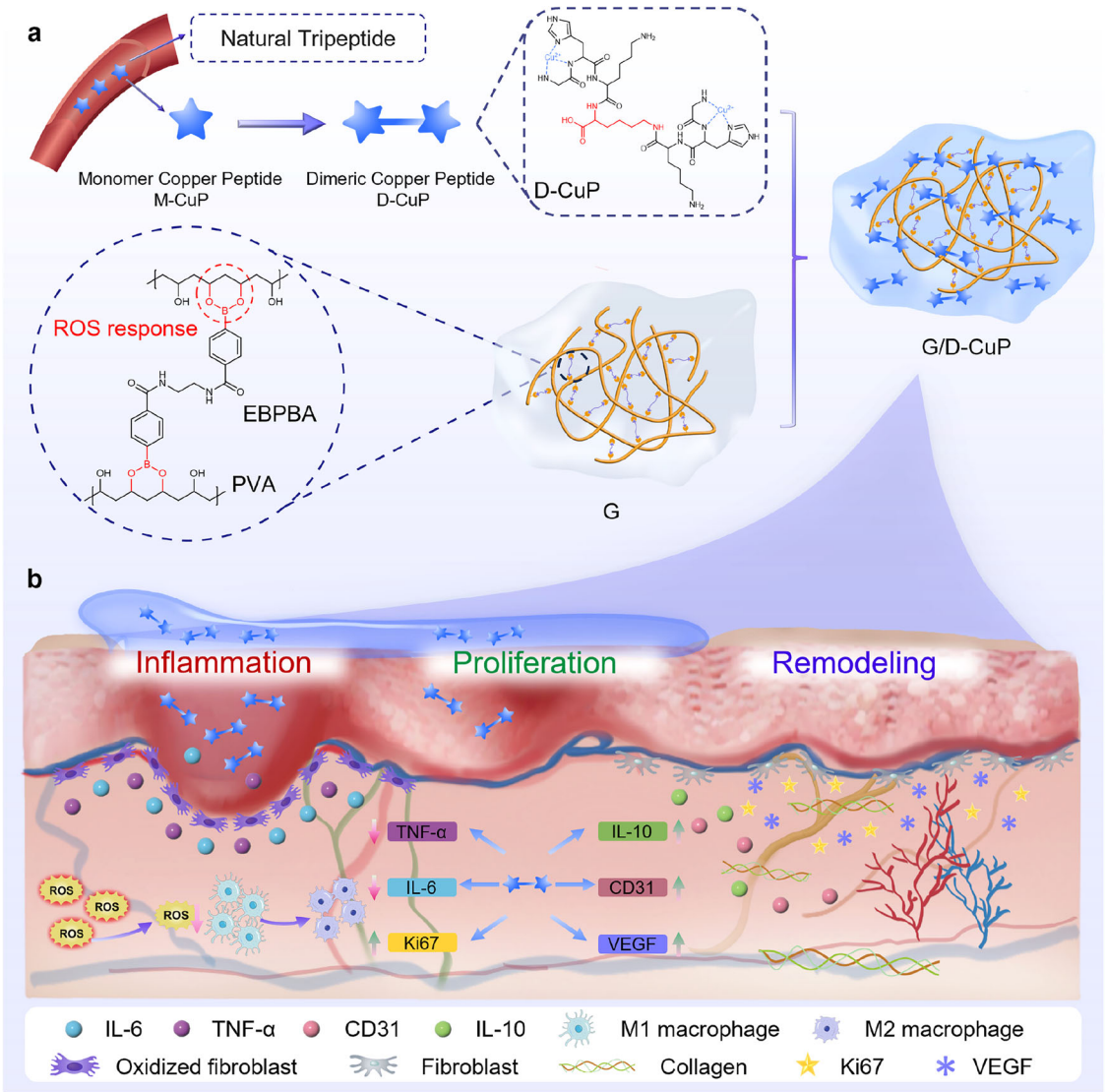

Fig. 1 | Dimeric copper-peptide incorporated hydrogel (G/D-CuP) for enhanced diabetic wound healing efficacy. a Illustration of the G/D-CuP production method. **b** The function of the G/D-CuP in the process of diabetic wound healing.

structure and elasticity disruption under high strain conditions with subsequent recovery. The hydrogel's ability to self-repair was also demonstrated in Fig. 3f, where it healed after being cut into two pieces and withstood bending force without cracking. Effective wound filling and infection prevention are crucial, especially in cases of irregularly shaped wounds[60,61]. Figure 3g and Supplementary Fig. 9 illustrated the hydrogel's ability to effectively spread and fill intricate star-shaped wounds. Supplementary Fig. 10 also evidenced the hydrogel's strong adhesion capabilities enable close contact with wound tissue, which was beneficial to prevent bacterial infiltration. Through cleavage of dynamic phenylboronic ester bonds under ROS stimulation[62], the hydrogel demonstrated ROS-sensitive drug release behavior, as evidenced by the 90% cumulative release of D-CuP within 72 h under H_2O_2 stimulation (Fig. 3h). To evaluate the stability and retention of G/D-CuP in vivo, it was topically applied to full-thickness dorsal wounds in diabetic mice. Dynamic imaging was performed at different times to monitor the morphological change of hydrogel. The results showed that the hydrogel remained at the wound site for over 48 h, indicating favorable retention (Supplementary Fig. 11a). Weight loss analysis of retrieved hydrogels showed 87.44% degradation within 48 h (Supplementary Fig. 11b). To assess drug release, we applied FITC-conjugated D-CuP hydrogel to the wounds and measured the fluorescence signal of the residual hydrogel at predetermined time intervals in darkness. As shown in Supplementary Fig. 11c, the results indicated a rapid initial release, with 56.79% released within the initial 12 h, followed by gradual and continuous release reaching a cumulative payload liberation of 91.12% at 48 h. These findings comprehensively address the in vivo stability, retention, and drug release properties of the G/D-CuP hydrogel, supporting its potential for therapeutic applications. Overall, G/D-CuP demonstrated superior mechanical properties like self-healing, strong adhesion, high malleability, and ROS responsiveness, making it a promising candidate for complex wound healing therapies.

In vitro anti-inflammatory effects and antioxidant capacity of the G/D-CuP

We evaluated the cellular uptake efficiency of D-CuP. As shown in Supplementary Fig. 12, fluorescence image analysis demonstrated that D-CuP achieved enhanced cellular internalization. Quantitative flow cytometry analysis indicated that D-CuP exhibited nearly 3.6-fold higher intracellular uptake compared to M-CuP, highlighting its capability for cellular entry by multivalency. Wound healing is a complicated process. High levels of ROS, excessive inflammatory cells and cytokines in the wound microenvironment, insufficient new blood vessels, and weakened cell proliferation are the key factors that lead to

https://doi.org/10.1038/s41467-025-61141-1

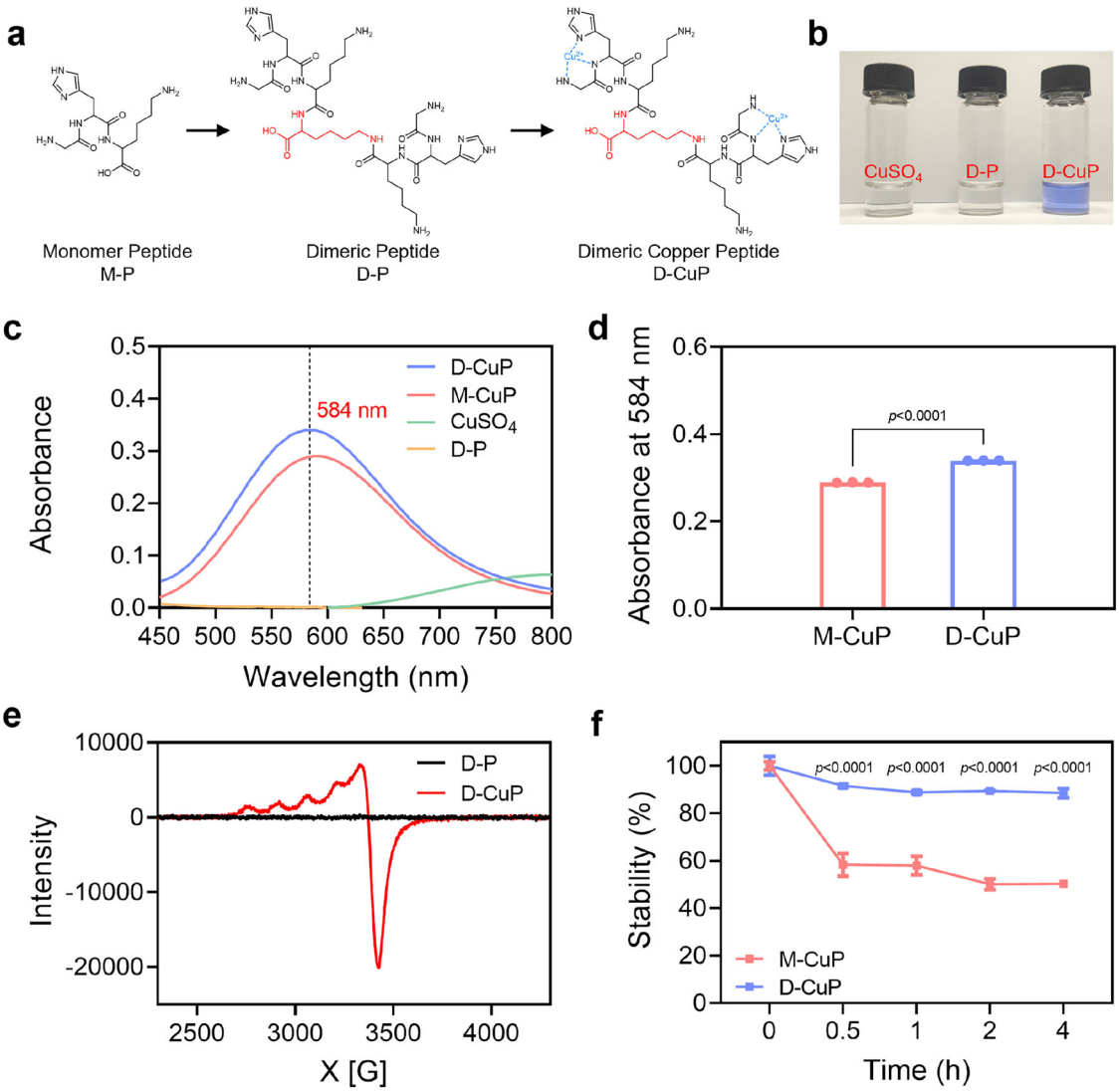

Fig. 2 | Preparation and characterization of the D-CuP. a Structural formula of the D-CuP. **b** The color of D-CuP solution. **c**, **d** UV-vis absorption spectra of D-CuP (n = 3 independent replicates). Statistical significance was assessed using unpaired t test. **e** Electron paramagnetic resonance spectroscopy of D-CuP. **f** Stability curve of M-CuP and D-CuP against protease K. Data represented as Mean ± SD (n = 3 independent replicates). Statistical significance was assessed using two-way ANOVA with Šídák's multiple comparisons test. Source data are provided as a Source Data file.

the difficult healing of diabetic wounds[24]. G/D-CuP was engineered to exert therapeutic effects across all phases of wound repair while targeting diverse pathological mechanisms, hence in vitro effects were validated. Macrophages exhibit a heterogeneous and plastic phenotype, capable of polarizing into the pro-inflammatory M1 or the reparative and anti-inflammatory M2 phenotypes. However, in diabetic wounds, the transition from M1 to M2 is disrupted, leading to the accumulation of M1 macrophages, which produce ROS and sustain long-term inflammation. As crucial regulators of local immune responses and tissue repair, macrophages in diabetic wounds show dysregulated switching from M1 to M2, resulting in a poor regenerative environment, exacerbated tissue damage, and delayed wound healing[63]. Firstly, CD206 was employed as the M2 macrophage marker to confirm macrophage polarization status using immunofluorescence staining performed under inflammatory stimuli (LPS and IFN-γ). The M1 phenotype, stimulated by lipopolysaccharide (LPS) and interferon-γ (IFN-γ), was used as a positive control, whereas the M2 phenotype, induced by interleukin-4 (IL-4), functioned as a negative control. As illustrated in Fig. 4a, the G/D-CuP group exhibited the most intense CD206-associated red fluorescence signal among all treatment groups, indicating that G/D-CuP promotes macrophage polarization toward the M2 phenotype. Furthermore, flow cytometry detected the changes of M1 (CD86 marker) and M2 (CD206 marker) macrophage phenotypes after various treatments. Upon treatment of LPS and IFN-γ stimulated M1 macrophages with G/D-CuP, the population of M1 macrophages reduced to 36.4% (Fig. 4b), while the population of M2 macrophages increased to 12.2%. The further analysis showed that G/D-CuP could significantly enhance the transition of macrophage phenotypes from M1 to M2 (Fig. 4c, d), suggesting an improvement in anti-inflammatory capacity. D-CuP also showed a better effect on the transition of macrophage phenotypes effect than M-CuP. Next, we used the pro-inflammatory cytokines tumor necrosis factor-α (TNF-α) and interleukin-6 (IL-6) as indicators to evaluate the anti-inflammatory response. As illustrated in Fig. 4e, f, both G/D-CuP and D-CuP exhibited a significant reduction in the expression levels of pro-inflammatory cytokines. In chronic diabetic wounds, uncontrolled accumulation of reactive oxygen species (ROS) leads to localized irreversible oxidative damage and heightened inflammation[64]. The ability of G/D-CuP to scavenge reactive oxygen species (ROS) was evaluated by conducting Fenton-like reactions where hydrogen peroxide (H_2O_2) generates reactive hydroxyl radicals (•OH) with the help of metal catalysts, leading to significant oxidative harm[65]. As illustrated in Supplementary

https://doi.org/10.1038/s41467-025-61141-1

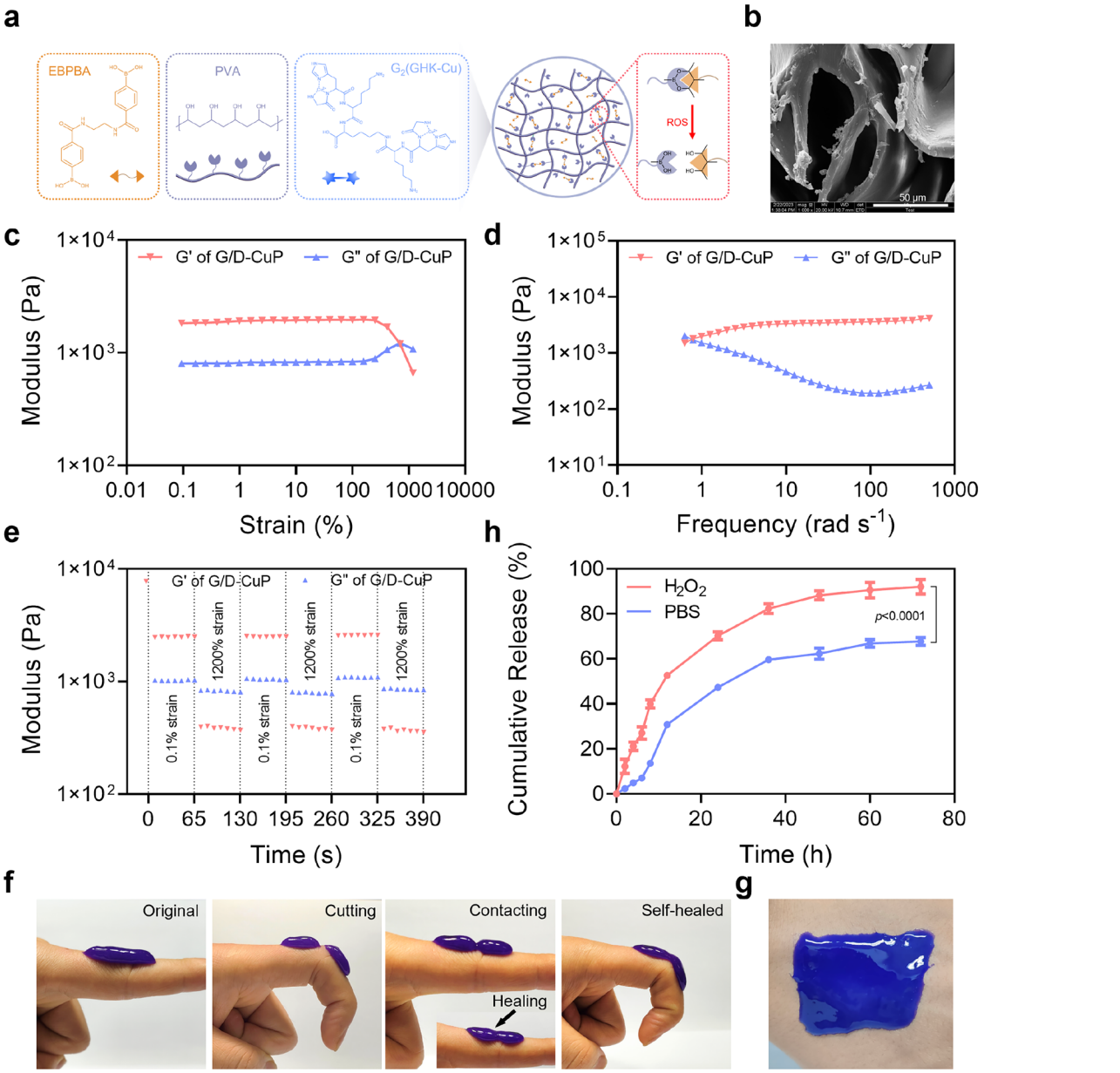

Fig. 3 | Characterization of the G/D-CuP. a The preparation process of G/D-CuP. **b** Representative SEM image of the G/D-CuP (Scale bars = 50 μm). Rheology study of G/D-CuP, **c** Strain-sweep, **d** Frequency-sweep, **e** Continuous step strain. **f** Self-healing property of G/D-CuP. **g** The malleability of G/D-CuP. **h** Cumulative release curves of G/D-CuP under PBS and H_2O_2 conditions. Data represented as Mean ± SD (n = 3 independent replicates). Statistical significance was assessed using two-way ANOVA with Šídák's multiple comparisons test. Source data are provided as a Source Data file.

Fig. 13, the ROS scavenging ratio of G/D-CuP exceeded 95% at different concentrations, indicating a potential beneficial antioxidant effect for treating diabetic wounds. To further assess the ROS scavenging ability of G/D-CuP, the 2′, 7′-dichlorofluorescein diacetate (DCFH-DA) fluorescent probe was used to measure intracellular ROS levels. As shown in Fig. 4g, the negative control group (NC) exposed to H_2O_2 exhibited strong green fluorescence, while the hydrogel-treated group displayed weak green fluorescence similar to the blank control group (BC) without H_2O_2. The groups receiving uncross-linked PVA or EBPBA solution showed no significant difference relative to the NC group, emphasizing the importance of phenylboronic ester bonds for scavenging ROS. M-CuP has antioxidant activity by increasing antioxidant enzymes and superoxide dismutase (SOD) activity, mainly neutralizing ROS by scavenging harmful oxygen-derived free radicals[66]. The dimeric copper peptide D-CuP showed superior antioxidant properties compared to M-CuP, leading to a notable decrease in relative fluorescence intensity. The mean fluorescence intensity for ROS-responsive hydrogel with monomer copper peptides M-CuP (G/M-CuP) and G/D-CuP groups decreased by 71% and 63%, respectively, in comparison to the NC group (Supplementary Fig. 14). SOD, a critical endogenous antioxidant enzyme, mitigates oxidative stress by catalyzing the dismutation of superoxide radicals via redox cycling, thus maintaining redox homeostasis[67]. The G/D-CuP group exhibited a markedly elevated SOD activity compared to the G/M-CuP group, indicating improved antioxidant capacity (Fig. 4h). The multivalency of the dimeric peptide structure contributes to the notable ROS-scavenging efficacy of G/D-CuP, confirming its great antioxidant capacity. These findings further validate the extraordinary antioxidant capacity of G/D-CuP, emphasizing its promise for use in wound repair. Hemocompatibility of the G/D-CuP was tested using a hemolysis assay. In Fig. 4i, the positive control (PC) group exhibited an intense red coloration, suggesting substantial erythrocyte lysis and hemoglobin

https://doi.org/10.1038/s41467-025-61141-1

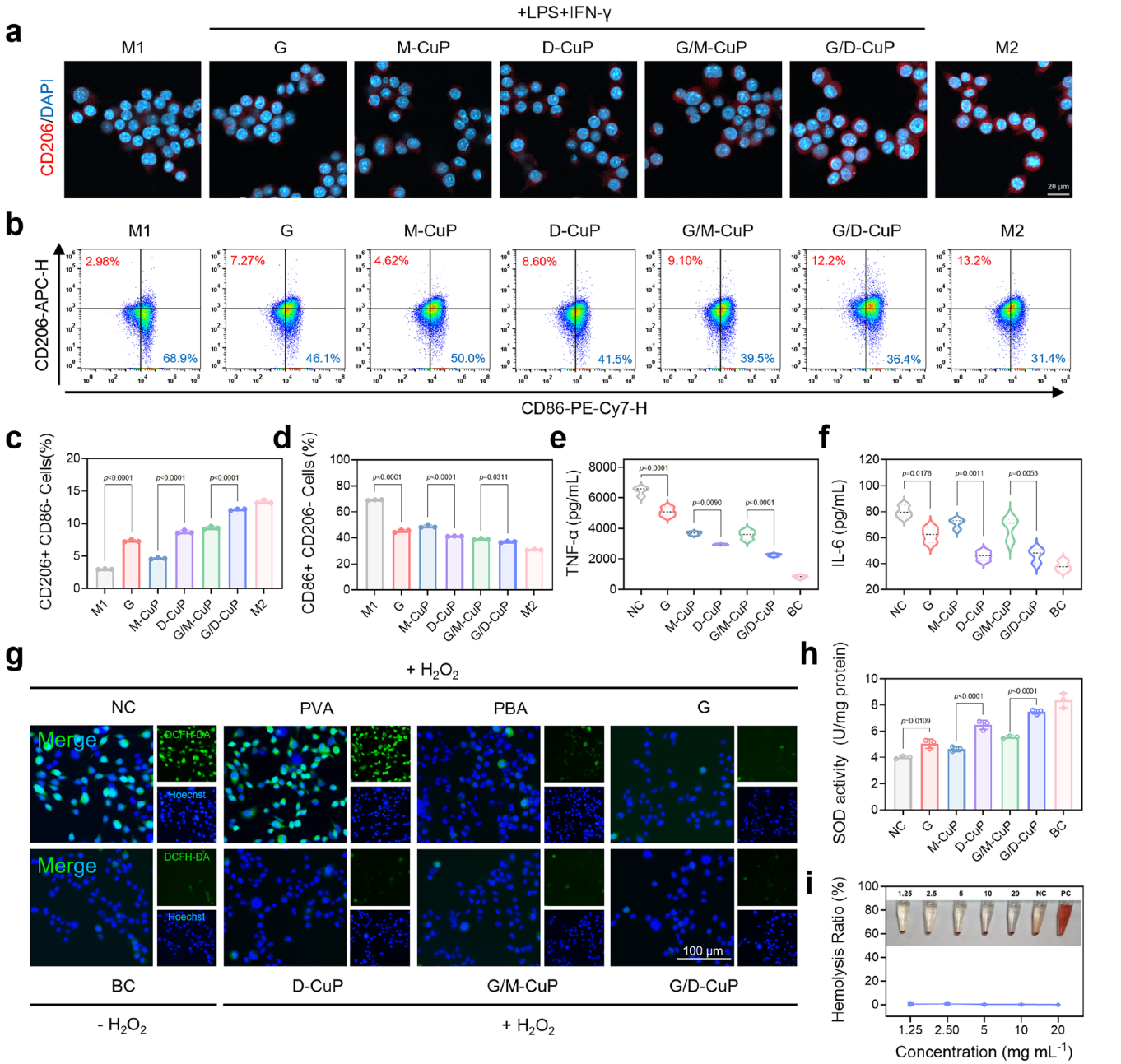

Fig. 4 | In vitro anti-inflammatory effects and antioxidant capacity of the G/D-CuP. a Representative fluorescent image of the macrophage phenotypes after different treatments (red: CD206; blue: cell nucleus) (Scale bars = 20 μm). **b** Flow cytometry analysis of CD206 and CD86 expression of RAW 264.7 cells after different treatments. Statistical analysis of (**c**) M1(CD86 + , CD206-) or (**d**) M2(CD206 + , CD86-) phenotype macrophages. Data represented as Mean ± SD (n = 3 independent replicates). Statistical significance was assessed using one-way ANOVA with Tukey's multiple comparisons test. The concentrations of (**e**) TNF-α, (**f**) IL-6 were determined by ELISA. Data represented as Mean ± SD (n = 3 independent replicates). Statistical significance was assessed using one-way ANOVA with Tukey's multiple comparisons test. **g** The ROS fluorescence images of NIH-3T3 cells after treatment with G/D-CuP. (Scale bars = 100 μm) (NC negative control group, BC blank control group). **h** Detection of SOD activities in NIH-3T3 cells after treatment with G/D-CuP. Data represented as Mean ± SD (n = 3 independent replicates) (NC negative control group, BC blank control group). Statistical significance was assessed using one-way ANOVA with Tukey's multiple comparisons test. **i** Hemolysis ratio of G/D-CuP. Data represented as Mean ± SD. (n = 3 independent replicates) (PC positive control group, NC negative control group). Source data are provided as a Source Data file.

release. In sharp contrast, neither the negative control (NC) group nor the G/D-CuP group exhibited any discoloration, suggesting hemolysis rates below 5% for these groups.

In vitro promotion of cell proliferation, migration and angiogenesis effects of the G/D-CuP

The formation of new blood vessels, called angiogenesis, is a crucial event during the proliferation stage of wound healing, and poor vascularization contributes to the delayed healing of diabetic wounds. This process entails endothelial cell proliferation, migration, and the formation of capillary-like tubular structures[68]. Immunofluorescence staining of Ki67, a marker for proliferating cells, was used to assess the proliferation of human umbilical vein endothelial cells (HUVECs)[63]. As shown in Fig. 5a, treatment with G/D-CuP elevated the number of Ki67-positive cells. Quantitative analysis of Ki67-positive cells showed that HUVEC proliferation after incubation with G/D-CuP was 69%,

https://doi.org/10.1038/s41467-025-61141-1

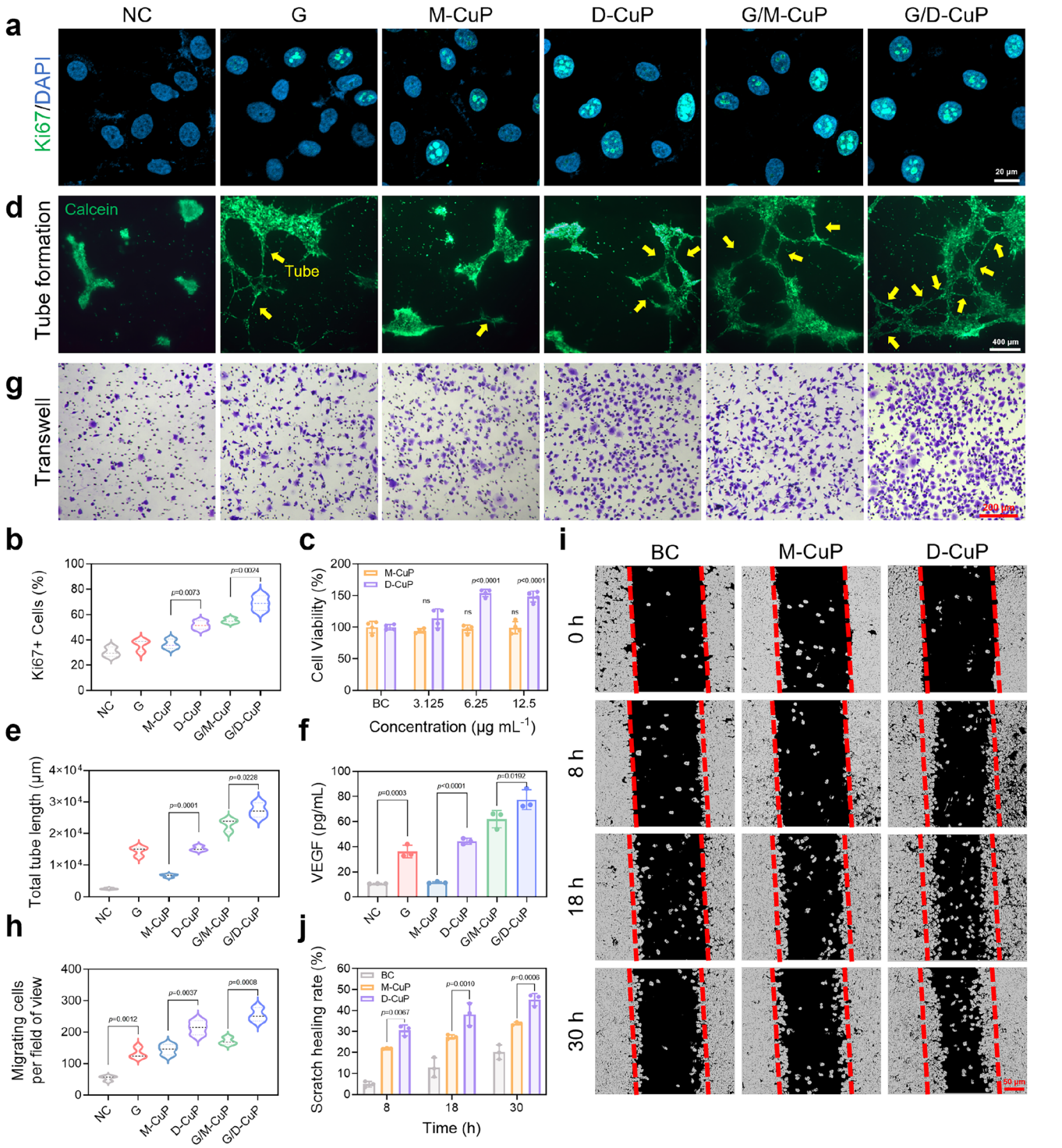

Fig. 5 | In vitro promotion of cell proliferation, migration, and angiogenesis effects of the G/D-CuP. a Representative fluorescence images of Ki67 staining of HUVEC cells after different treatments (green: Ki67; blue: cell nucleus, Scale bars = 20 μm). **b** Quantitative analysis of Ki67+ cells. Data represented as Mean ± SD (n = 3). Statistical significance was assessed using one-way ANOVA with Tukey's multiple comparisons test. **c** Relative cell viability of NIH/3T3 cells co-cultured with D-CuP solution and M-CuP solution for 24 h. Data represented as Mean ± SD (n = 4 independent replicates, ns not significant). Statistical significance was assessed using two-way ANOVA with Tukey's multiple comparisons test. **d** Representative images of tube formation assay in HUVEC cells stained with calcein-AM (green) (Tube: yellow arrow, Scale bars = 400 μm). **e** Quantitative analysis of total tube length. Data represented as Mean ± SD (n = 3). Statistical significance was assessed using one-way ANOVA with Tukey's multiple comparisons test. **f** The concentrations of VEGF were determined by ELISA. Data represented as Mean ± SD (n = 3 independent replicates). Statistical significance was assessed using one-way ANOVA with Tukey's multiple comparisons test. **g** Representative images of transwell migration assay of L929 cells (Scale bars = 200 μm). **h** Quantitative analysis of total tube length. Data represented as Mean ± SD (n = 3). Statistical significance was assessed using one-way ANOVA with Tukey's multiple comparisons test. **i** Images of L929 cells scratch experiment after incubating with D-CuP or M-CuP at different times (Scale bars = 100 μm). **j** Cell scratch healing rates at different times. Data represented as Mean ± SD (n = 3 independent replicates). Statistical significance was assessed using two-way ANOVA with Tukey's multiple comparisons test. Source data are provided as a Source Data file.

significantly higher than that of other groups (Fig. 5b). Fibroblasts synthesize extracellular matrix (ECM) components, glycoproteins, adhesion molecules, and a range of cytokines. Their ability to migrate, proliferate, and secrete ECM is essential for effective dermal tissue regeneration[69]. The proliferative activity towards fibroblasts was also evaluated using the MTT assay. As depicted in Fig. 5c and Supplementary Figs. 15, 16, D-CuP, ROS-responsive hydrogel matrix (G) and G/D-CuP demonstrated good biocompatibility. Compared to M-CuP, D-CuP exhibited significantly higher proliferative activity at lower concentrations, which was more conducive to wound healing. To assess the G/D-CuP's biocompatibility and its ability to support cell growth, we performed in vitro three-dimensional (3D) culture experiments using NIH/3T3 cells as a model. After 24 h of co-culture with G/D-CuP, NIH/3T3 cells displayed well-spread morphology and high viability, as demonstrated by both 3D and 2D Calcein-AM fluorescence imaging via CLSM (Supplementary Fig. 17). These findings confirmed that G/D-CuP provides a supportive 3D microenvironment for fibroblast survival and proliferation, highlighting its potential for chronic wound healing and tissue regeneration.

An endothelial tube formation was also evaluated. As shown in Fig. 5d, e and Supplementary Fig. 18, a substantial number of blood vessel structures were observed in the G/D-CuP group, with both tube length and the number of meshes significantly higher than those in other treatment groups. Vascular endothelial growth factor (VEGF) functions as a powerful mitogen for endothelial cells and a crucial regulator of angiogenesis[70]. ELISA results of VEGF further displayed that G/D-CuP enhanced the ability of angiogenesis (Fig. 5f). Overall, G/D-CuP demonstrated an ability to promote neovascularization, thereby accelerating wound healing.

Impaired cell migration, as a critical factor, affects diabetic wound healing during the proliferative and remodeling phases. To evaluate the cell migration, a transwell assay was conducted. Apparently, G/D-CuP significantly promoted fibroblast migration (Fig. 5g, h). For a more detailed understanding of the wound repair efficacy, an in vitro scratch assay was carried out using L929 cells. Wound closure was simulated and observed for 30 h following treatment of the scratched cell monolayer with M-CuP or D-CuP. As shown in Fig. 5i, j, cell migration was elevated in all treatment groups relative to the control. Notably, D-CuP exhibited faster cell migration than M-CuP. The increased efficacy is likely due to the enhanced stability and boosted bioactivity of D-CuP throughout the scratch wound repair process. The above findings indicate that D-CuP exhibits good biocompatibility, hemocompatibility, anti-inflammatory, antioxidant capabilities, and promotes cell proliferation, migration and angiogenesis.

Proteomics analysis of therapeutic performance of D-CuP

To elucidate the regulatory mechanisms of D-CuP, we conducted a quantitative proteomics analysis on murine L929 fibrosarcoma cells before and after treatment under nutrient stress (Fig. 6a). Initially, the alterations in intracellular protein concentrations post-treatment were assessed, and the principal component analysis (PCA) outcomes demonstrated a notable divergence in protein expression between the D-CuP-treated group and the PBS-treated control group (Fig. 6b). Compared to the PBS-treated control group, the D-CuP-treated group exhibited 74 differentially expressed proteins (DEPs), consisting of 29 upregulated and 45 downregulated proteins ($p < 0.05$, fold change ratio >1.2) (Fig. 6c). We categorized the primary differential proteins into three phases of wound healing: inflammatory, proliferative, and remodeling (Fig. 6d). Specifically, proteins associated with DNA damage, inflammation, and oxidative stress, including Cop1, H2-D1, Ndufa6, and Fam76a, showed downregulation following D-CuP treatment. Moreover, the levels of proteins associated with cell proliferation, migration, and angiogenesis (Slc38a2, Psph, Jagn1, and Rorb) were upregulated. A Gene Ontology (GO) functional enrichment analysis of differentially expressed proteins (DEPs) was also carried out, as depicted in Fig. 6e and Supplementary Fig. 19. The analysis revealed that within the molecular function category, molecular function regulator and transporter activity were prominent. In the cellular component category, cell and membrane were dominant. Moreover, within the biological process category, cellular process, regulation of biological process, and biological regulation were identified as key processes. Furthermore, Kyoto Encyclopedia of Genes and Genomes (KEGG) pathway enrichment analysis of DEPs mainly included nucleotide excision repair and p53 signaling pathway (Fig. 6f). Additionally, the mTOR, IL-17, NOD-like receptor and HIF-1 signaling pathways were involved (Supplementary Fig. 20). These findings suggest that D-CuP exhibits anti-inflammatory and antioxidant properties, enhances cell proliferation and migration, and thereby supports diabetic wound healing. To further elucidate the therapeutic mechanisms underlying D-CuP's multivalent interactions, comprehensive proteomic analysis revealed two pivotal transcriptional regulators, the tumor suppressor protein p53 and histone deacetylase 7 (HDAC7) to be potential mechanistic targets. Downregulation of the p53 signaling pathway promotes cellular proliferation and modulates inflammatory responses[71], while HDAC7 depletion facilitates cell migration, angiogenesis, and extracellular matrix remodeling, collectively contributing to coordinated tissue repair[72]. To evaluate the target-binding capacity of D-CuP, molecular docking simulations were conducted using AutoDock Vina against the functional domains of p53 (DNA-binding domain) and HDAC7 (catalytic deacetylase domain). Comparative analysis showed that D-CuP exhibited higher binding affinities than its monomeric counterpart M-CuP, with Vina scores of -5.7 kcal/mol for p53 and -6.4 kcal/mol for HDAC7, compared to -4.2 kcal/mol and -4.8 kcal/mol for M-CuP, respectively (Fig. 6g). To further validate the multivalent interactions of D-CuP, SPR analysis was performed to quantify its binding ability to p53 and HDAC7 in comparison with M-CuP. As shown in Fig.6h, D-CuP exhibited significantly stronger binding affinities, with equilibrium dissociation constants (KD) of 3.8×10^{-6} M for p53 and 1.81×10^{-6} M for HDAC7. In contrast, M-CuP showed negligible binding to either target, with maximal responses below 5 response units (RU) across all tested concentrations, confirming the essential role of multivalent architecture in cooperative target engagement.

In vivo effects of the G/D-CuP

Motivated by the favorable biocompatibility, antioxidant capability, and the facilitation of fibroblast cell proliferation and migration, we evaluated the efficacy of G/D-CuP hydrogels for diabetic wound healing in vivo (Fig. 7a). To evaluate the healing efficacy, a comprehensive experiment was conducted on diabetic wounds treated with various agents, including: i) PBS as negative control (NC group), ii) ROS-responsive hydrogel matrix (G group), iii) monomer copper peptides M-CuP solution (M-CuP group), iv) dimeric copper peptides D-CuP solution (D-CuP group), v) ROS-responsive hydrogel with monomer copper peptides M-CuP (G/M-CuP group), and vi) ROS-responsive hydrogel with dimeric copper peptides (G/D-CuP group). Healthy mice wounds were treated with PBS as the blank control (BC group). Representative images of the wounds in various groups from days 0 to 12 were depicted in Fig. 7b, c. Macroscopically, wound healing was delayed in diabetes, and abscesses were observed in the NC group. All groups exhibited a significant reduction in wound area after 3 days of treatment compared to the NC group. G/D-CuP exhibited a specific decrease in wound area from 100% to 17.3% after 7 days (Fig. 7d), surpassing the reduction observed in the other groups. Notably, on day 12, significantly large wound areas remained in both the NC and M-CuP groups, comprising 34.2% and 17.8%, respectively. Conversely, the D-CuP group demonstrated enhanced wound healing, leaving a residual wound area of just 9.8%, while the G/D-CuP group exhibited the most pronounced wound healing, with only 2.8% of the wound area remaining. Histological analysis was further conducted on days 7 and

https://doi.org/10.1038/s41467-025-61141-1

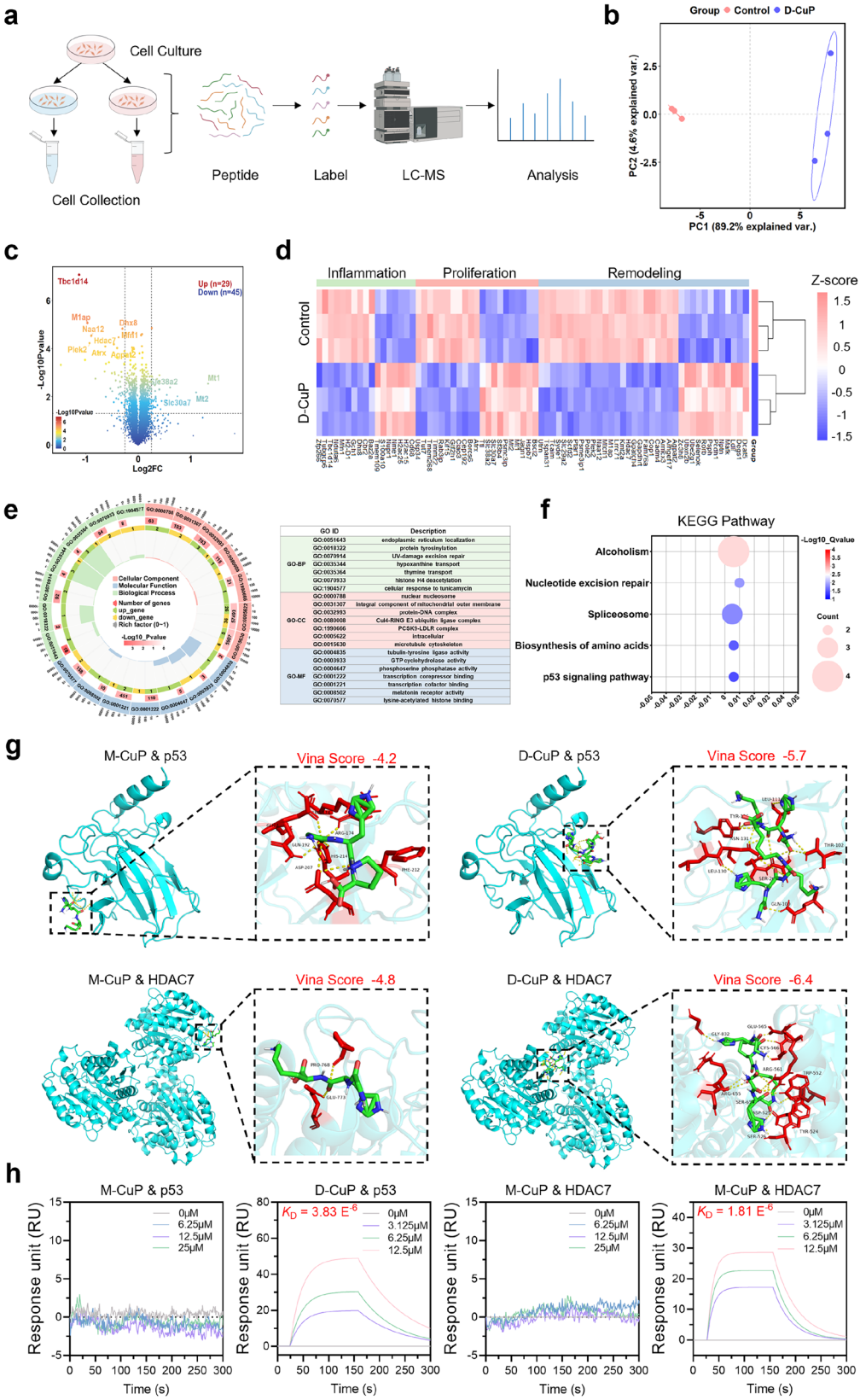

Fig. 6 | Proteomics assessment of L929 cells before and after D-CuP treatment. **a** Diagrammatic sketch of proteomic analysis. **b** Principal component analysis (PCA) was performed based on differentially expressed proteins (DEPs) in the L929 cells of the two groups. **c** Volcano plots showing the upregulated and downregulated genes in response to D-CuP treatment. Statistical significance was assessed using Student's t test. **d** Heat map of upregulated and downregulated proteins. (fold change ratio >1.2 and p <0.05). Statistical significance was assessed using Student's t test. **e** GO function analysis of DEPs between D-CuP-treated and the control cells. **f** KEGG enrichment for the DEPs between D-CuP-treated and the control cells. **g** Pattern diagram illustrating the molecular docking interactions between p53 and M-CuP, p53 and D-CuP, HDAC7 and M-CuP, and HDAC7 and D-CuP. **h** SPR analysis of the binding affinities of M-CuP and D-CuP with p53 or HDAC7. Source data are provided as a Source Data file.

https://doi.org/10.1038/s41467-025-61141-1

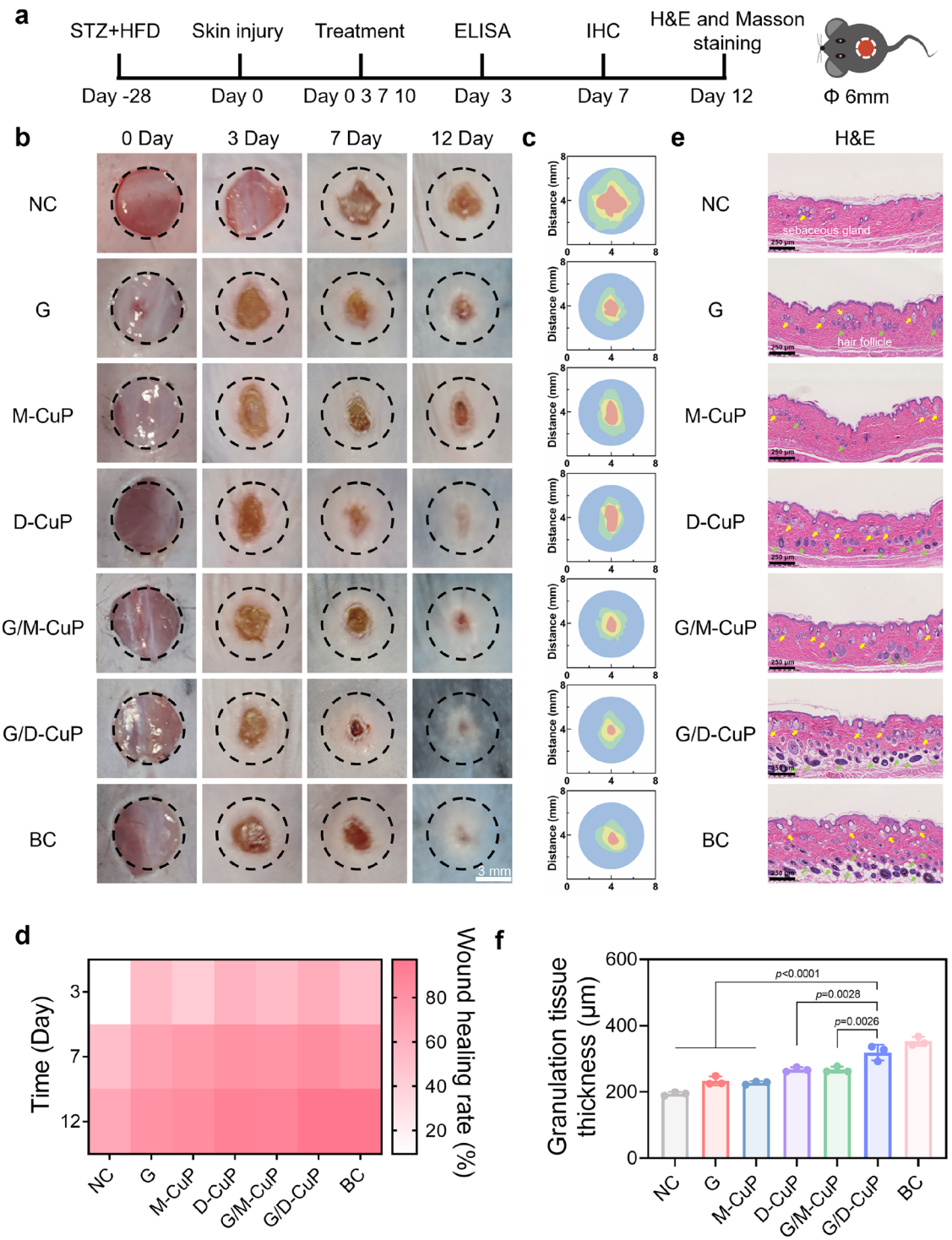

Fig. 7 | Effects of the G/D-CuP in promoting diabetic wound healing. a Schematic illustration of the timeline of animal experiments to test the therapeutic effect of different groups. **b** Representative photographs of the wounds in different treatment groups (Scale bar = 3 mm). **c** Portions of wounds healed under various treatments on days 0, 3, 7, and 12. **d** Wound healing rate within 12 days. **e** H&E staining of wound tissue with different treatments on the 12th day (sebaceous glands: yellow arrow, hair follicles: green arrow. Scale bar = 250 μm). **f** Granulation tissue thickness in each group on the 12th day. Data represented as Mean ± SD (n = 3 independent replicates). Statistical significance was assessed using one-way ANOVA with Tukey's multiple comparisons test. Source data are provided as a Source Data file.

12 to evaluate the quality of the regenerated skin. The H&E staining results (Fig. 7e and Supplementary Fig. 21) showed that the wound treated with G/D-CuP exhibited complete recovery, characterized by densely arranged granulation tissue, as well as increased the presence of skin appendages, including hair follicles (HFs) and sebaceous glands. As shown in Fig. 7f, the G/D-CuP also enhanced the thickness of granulation tissue, thereby enhancing diabetic wound healing. G/D-CuP facilitates the proliferation of dermal papilla cells, reduces their apoptosis, fosters hair follicle growth and regeneration, and enhances wound healing. Moreover, an increased recruitment of adipocytes to the wound site further supports simultaneous tissue regeneration[37].

The effect of the G/D-CuP on the inflammation, proliferation, and remodeling stages of tissue repair was also assessed. The initial inflammatory phase of wound healing, typically lasting 2–3 days in physiological wounds, is extended in chronic wounds[73]. This phase is consistently characterized by elevated levels of inflammatory cytokines. To evaluate levels of inflammatory cytokines, expression levels of interleukin-6 (IL-6) and interleukin-10 (IL-10) were measured by ELISA after three days of treatment. In diabetic wounds, the G/D-CuP group exhibited lower IL-6 expression and higher IL-10 expression compared to the G/M-CuP group (Fig. 8a, b), suggesting a shorter inflammatory phase after G/D-CuP treatment. Histological analysis on day 7 revealed a significant decrease in the expression of proinflammatory cytokines in the wound, including TNF-α and IL-6 in the D-CuP groups, accompanied by an increase in IL-10 expression (Fig. 8c and Supplementary Fig. 21). This result indicated that dimeric copper peptides can accelerate the switch from the inflammatory to the proliferative phase by regulating the expression of inflammatory factors. G/D-CuP could have superior efficacy in modulating inflammatory factors compared to G/M-CuP, likely due to the multivalency effect of dimeric copper peptides, which enhanced the activity.

Immunofluorescence staining was performed to assess macrophage polarization, with CD86 serving as a marker for proinflammatory M1 macrophages and CD206 for anti-inflammatory M2 macrophages. As shown in Supplementary Fig. 22, the G/D-CuP group showed a significantly lower proportion of CD86-positive cells compared to the negative control (NC) group. Notably, the G/D-CuP group demonstrated the lowest CD86/CD206 ratio, further indicating a promoted transition from the M1 to M2 phenotype (Supplementary Fig. 23). Together, these findings suggest that G/D-CuP promotes macrophage polarization toward the M2 phenotype, thereby reducing inflammation, enhancing antioxidant capacity, and ultimately accelerating effective wound healing. As shown in Supplementary Fig. 22, G/D-CuP group exhibited a significantly reduced proportion of CD86-positive cells compared to the NC group. Notably, the G/D-CuP group showed the lowest ratio of CD86-positive macrophages/CD206-positive macrophages, indicating an enhanced M1-to-M2 transition (Supplementary Fig. 23). Immunofluorescence staining and semi-quantitative analysis demonstrated that the G/D-CuP group significantly upregulated SOD expression compared with the G/M-CuP group (Supplementary Figs. 24, 25). Collectively, these findings suggest that G/D-CuP facilitates macrophage phenotype switching and enhances antioxidant capacity, thereby mitigating inflammation and ultimately accelerating effective wound healing.

During the proliferation phase, neovascularization is essential for delivering nutrients and oxygen to the wound site, thereby promoting fibroblast proliferation, collagen synthesis, and re-epithelialization[73]. Vascular endothelial growth factor (VEGF), a typical marker of angiogenesis during wound healing, was quantitatively assessed via ELISA on day 3, revealing a significant increase in the G/D-CuP group (Fig. 8d). Immunohistochemical analysis shown in Fig. 8c, e, Supplementary Figs. 21 and 26 illustrated a substantial elevation in the expression of both VEGF and platelet endothelial cell adhesion molecule-1 (CD31) on day 7 after treatment with G/D-CuP, compared to the negative control and Gel groups. Specifically, quantitative analysis revealed that the relative average density (AOD) of CD31 was 1.48-fold higher in the G/D-CuP group than in the G/M-CuP group. The initiation of vascularization at an earlier stage of wound healing can result in a faster rate of wound closure. However, excessive vascularization during the mid-phase of wound healing impedes fibroblast growth and wound tissue re-epithelialization[74]. Furthermore, excessive vascularization during wound healing may lead to adverse outcomes, such as wound fibrosis and scar formation. On the 12th day, the G/D-CuP group exhibited significantly fewer blood vessels, while CD31 expression persisted in the M-CuP and G/M-CuP groups. This suggested that wound healing was nearly complete in the G/D-CuP group with minimal new blood vessel formation on day 12, whereas the M-CuP and G/M-CuP groups, still in the healing process, exhibited increased angiogenesis. These findings indicate that G/D-CuP may significantly promote angiogenesis, as evidenced by increased CD31 expression during the initial stages of wound healing. Consequently, G/D-CuP has the potential as a wound dressing to expedite the remodeling phase onset and mitigate excessive vascularization.

During the remodeling phase, cell proliferation, proper collagen deposition, and remodeling play crucial roles in enhancing tissue tensile strength and facilitating improved healing[75]. Ki67, a key marker of cell proliferation, was examined in wound samples on day 7 and day 12 to evaluate cell proliferation. Immunostaining results showed an increase in Ki67 expression in the G/D-CuP group compared to other groups, while the control group exhibited minimal positive cells on day 7 (Fig. 8c, f, Supplementary Figs. 21 and 26). Interestingly, this pattern reversed on day 14, with delayed proliferative fibroblastic cells in the NC group and few detected in the G/D-CuP group, indicating that the G/D-CuP treatment facilitates wound healing through a time-dependent mechanism. Masson's trichrome staining was utilized to evaluate collagen deposition within the wound healing site. Collagen fibers in the G/D-CuP group exhibited increased density, thickness, and organization compared to the G/M-CuP group, suggesting enhanced collagen deposition (Fig. 8g). These results highlight the superior wound healing ability of G/D-CuP, with healed tissue resembling healthy skin, surpassing outcomes from other treatments.

Discussion

Chronic diabetic wounds represent a huge healthcare challenge, necessitating sustained and synchronized regulation of the wound microenvironment simultaneously with tissue reconstruction processes. However, current wound management approaches face challenges in coordinating the individual management approaches within the disordered diabetic wound microenvironment. Therefore, developing a comprehensive therapeutic platform capable of spatiotemporal ROS scavenging, regulation of macrophage polarization, and enhancement of angiogenesis and cell proliferation represents a critical research focus for improving clinical outcomes in chronic diabetic wound management.

In this study, a multifunctional dimeric copper peptide incorporated hydrogel, G/D-CuP has been developed as an innovative wound dressing to promote diabetic wound healing. The hydrogel dressing comprised PVA, a ROS-responsive linker EBPBA, and dimeric copper peptide D-CuP. D-CuP exhibited multivalency, significantly enhancing biological activity and stability against proteases. The dynamic phenylboronic ester hydrogel, with ROS responsiveness and scavenging capabilities, helps alleviate inflammation and serves as a drug reservoir for the controlled release of D-CuP at the wound site. The hydrogel displayed repairability, malleability, and ideal mechanical strength, crucial for complex wound healing treatments. Notably, G/D-CuP exerted anti-inflammatory and antioxidative properties, promoting angiogenesis, fibroblast proliferation, and migration to accelerate wound healing without the need for additional bioactive substances. In vivo studies demonstrated that the G/D-CuP accelerated the three phases of diabetic wound repair (inflammation, proliferation, and remodeling). The G/D-CuP was also biocompatible, easily synthesized, and showed promise as a dressing material for managing diabetic wounds. Given the enhanced therapeutic efficacy of D-CuP, it is a potential substitute for M-CuP in wound repair, cosmetics, and other applications. Furthermore, the design presents a promising approach for leveraging bioactive linear peptides.

Methods

Ethics declarations

All the animal experiments were performed following the Guide for Care and Use of Laboratory Animals, approved by the Animal

https://doi.org/10.1038/s41467-025-61141-1

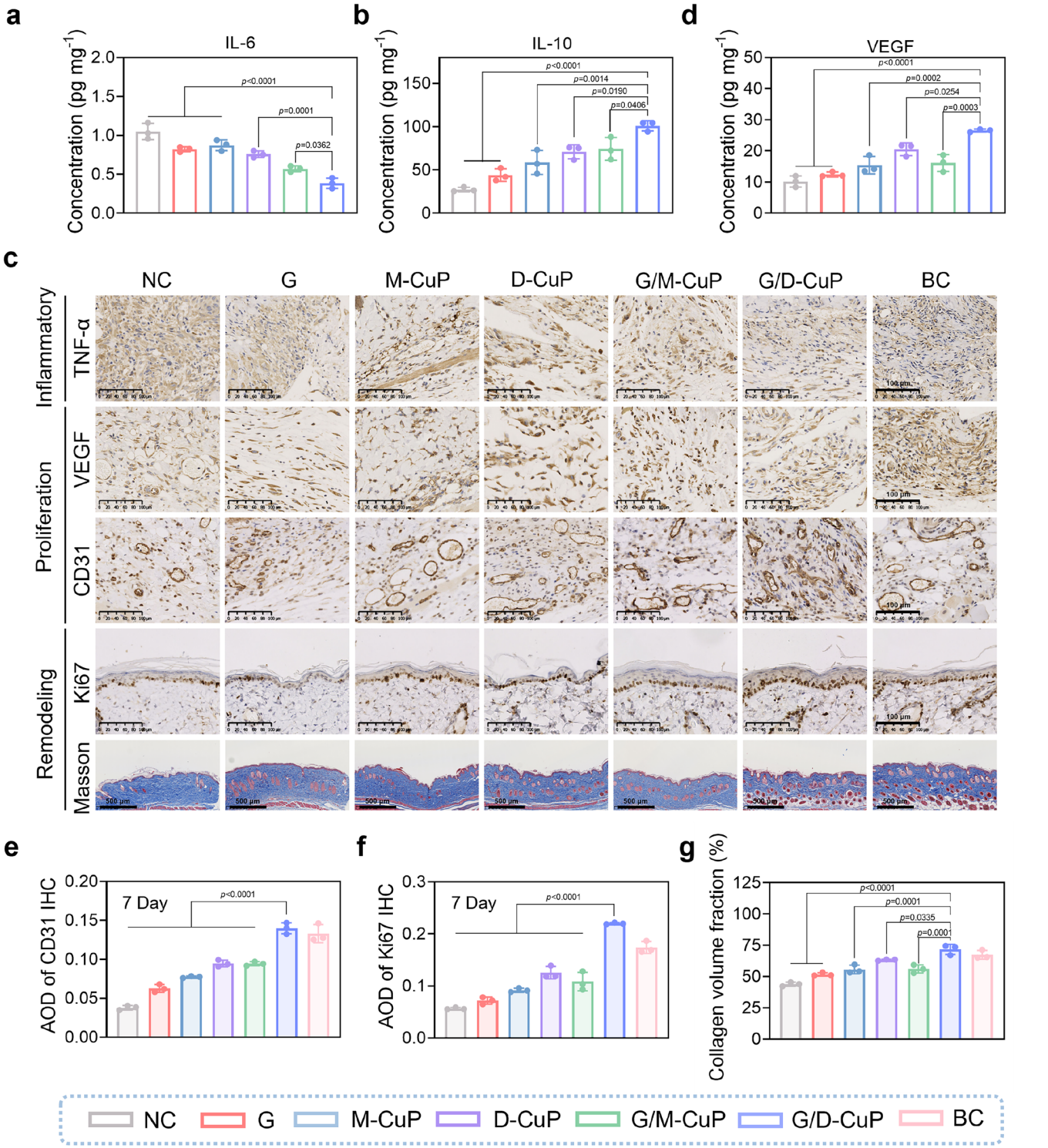

Fig. 8 | G/D-CuP-induced acceleration of the three phases of diabetic wound repair. The concentrations of (**a**) IL-6, (**b**) IL-10, and **d** VEGF in the wound tissue were determined by ELISA on day 3. Data represented as Mean ± SD. (n = 3 independent replicates) Statistical significance was assessed using one-way ANOVA with Tukey's multiple comparisons test. **c** Representative images of immunohistochemistry staining of TNF-α, VEGF, CD31, and Ki67 (Scale bars = 100 μm) on day 7 and Masson staining on day 12 (Scale bars = 500 μm). Quantitative analysis of immunohistochemical staining for (**e**) CD31 and (**f**) Ki67 on day 7. Data represented as Mean ± SD. (n = 3 independent replicates) Statistical significance was assessed using one-way ANOVA with Tukey's multiple comparisons test. **g** Quantification of the collagen deposition in different groups on day 12. Data represented as Mean ± SD (n = 3 independent replicates). Statistical significance was assessed using one-way ANOVA with Tukey's multiple comparisons test. Source data are provided as a Source Data file.

Experimentation Ethics Committee of China Pharmaceutical University (2022-10-017). This study involved only non-invasive application of a test hydrogel on the dorsal hand skin of a healthy adult volunteer for photographic documentation. The study did not involve any clinical procedures or personal data collection. According to the policy of the Animal Experimentation Ethics Committee of China Pharmaceutical University, such minimal-risk procedures are exempt from ethical approval. Written informed consent was

obtained from the participant for both participation and image publication.

Materials

H-His(Trt)-OMe·HCl, H-Lys(Boc)-OMe·HCl, H-Lys-OMe·2HCl, ((1H-Benzo[d][1,2,3]triazol-1-yl)oxy)tri(pyrrolidine-1-yl)phosphonium hexafluorophosphate(V) (PYBOP), 2-(1H-benzotriazole-1-yl)-1,1,3,3-tetramethyluronium hexafluorophosphate (HBTU), 1-hydroxy benzotriazole hydrate (HOBT), GHK and 4-carboxyphenyl boric acid were obtained from Bide Pharmatech Ltd (Shanghai, China). N, N-diisopropylethylamine (DIPEA), Protease K, 30% hydrogen peroxide (H_2O_2) solution, and Ethylenediamine dihydrochloride were purchased from Shanghai Aladdin Biochemical Technology Co., Ltd. (Shanghai, China). Fetal bovine serum (FBS) was purchased from VivaCell (Shanghai, China). Reactive Oxygen Species (ROS) kit, DAPI and Calcein AM were purchased from Beyotime Biotechnology Corp., Ltd. (Shanghai, China). DMEM high glucose medium and ELISA kits were purchased from Keygen Biotech Corp., Ltd. (Jiangsu, China). Streptozotocin (STZ) was purchased from OKA (Beijing, China). Matrigel was purchased from Yeasen Biotechnology Co., Ltd. (Shanghai, China).

Synthesis of D-P

H-His(Trt)-OMe·HCl (5.0 g, 11.15 mmol), Boc-Gly-OH (2.15 g, 12.25 mmol), HATU (8.5 g, 22.35 mmol) and HOAT (3.0 g, 22.35 mmol) were dissolved in DMF (80 mL) under nitrogen atmosphere and ice bath conditions. DIPEA (7.75 mL, 44.7 mmol) was slowly added to the mixture. The reaction mixture was stirred at room temperature for 24 h. After completion of the reaction, the solvent was removed under reduced pressure, and the residue was dissolved in ethyl acetate. The organic phase was washed three times sequentially with saturated $NaHCO_3$ (aq), 0.1 M HCl, and saturated NaCl (aq), respectively. The organic layer was dried over anhydrous Na_2SO_4, filtered, and concentrated under reduced pressure. Compound 1 was isolated by silica gel column chromatography using a dichloromethane/methanol (DCM:MeOH = 60:1, V/V) eluent (yield: 80%).

^{1}H NMR (300 MHz, DMSO) δ 8.26 (d, J = 7.6 Hz, 1H), 7.45 – 7.34 (m, 9H), 7.25 (d, J = 1.4 Hz, 1H), 7.13 – 7.03 (m, 6H), 7.03 – 6.95 (m, 1H), 6.70 – 6.61 (m, 1H), 4.49 (q, J = 6.9 Hz, 1H), 3.54 (s, 3H), 3.52 (d, J = 5.9 Hz, 1H), 2.82 (dd, J = 6.7, 3.4 Hz, 2H), 1.35 (s, 9H). MS (ESI) m/z: 568.27, found 569.28 $[M + H]^+$.

Compound 1 (6 g, 10.53 mmol) was dissolved in 50 mL MeOH with NaOH (2 g, 50 mmol) under ice bath conditions. The reaction mixture was stirred at room temperature for 6 h. After completion of the reaction, the pH was adjusted to pH = 2-3 with citric acid solution (pH = 2). The solvent was removed under reduced pressure. The residue was diluted with ethyl acetate and washed with saturated NaCl (aq). The organic layer was dried over anhydrous Na_2SO_4, filtered, and concentrated under reduced pressure to obtain Compound 2 (yield: 98%).

^{1}H NMR (400 MHz, DMSO) δ 8.74 (s, 1H), 8.22 (d, *J* = 8.3 Hz, 1H), 7.50 – 7.39 (m, 9H), 7.22 (s, 1H), 7.18 – 7.09 (m, 6H), 6.91 (t, *J* = 6.0 Hz, 1H), 4.57 (td, *J* = 9.0, 4.8 Hz, 1H), 3.50 (d, *J* = 10.9 Hz, 2H), 3.14 (dd, *J* = 15.0, 4.9 Hz, 1H), 2.94 (dd, *J* = 15.0, 9.8 Hz, 1H), 1.34 (s, 9H). MS (ESI) m/z:554.25, found 555.26 $[M + H]^+$.

Compound 2 (5.4 g, 9.72 mmol), H-Lys(Boc)-OMe·HCl (3.46 g, 11.52 mmol), HATU (7.42 g, 19.44 mmol) and HOAT (2.64 g, 19.44 mmol) were dissolved in DMF (80 mL) under nitrogen atmosphere and ice bath conditions. DIPEA (6.66 mL, 38.88 mmol) was slowly added into the mixture. The reaction mixture was stirred at room temperature for 24 h. After completion of the reaction, the solvent was removed under reduced pressure, and the residue was dissolved in ethyl acetate. The organic phase was washed three times sequentially with saturated $NaHCO_3$ (aq), 0.1 M HCl, and saturated NaCl (aq), respectively. The organic layer was dried over anhydrous Na_2SO_4, filtered, and concentrated under reduced pressure. Compound 3 was isolated by silica gel column chromatography using a dichloromethane/methanol (DCM:MeOH = 40:1, V/V) eluent (yield: 75%).

^{1}H NMR (300 MHz, DMSO) δ 8.23 (d, *J* = 7.4 Hz, 1H), 8.12 (d, *J* = 8.2 Hz, 1H), 7.41 (d, *J* = 6.6 Hz, 9H), 7.23 (s, 1H), 7.12 – 7.04 (m, 6H), 6.78 (d, *J* = 5.4 Hz, 1H), 6.67 (d, *J* = 11.0 Hz, 1H), 4.56 (d, *J* = 6.6 Hz, 1H), 4.14 (q, *J* = 7.4 Hz, 1H), 3.60 (s, 3H), 3.51 (d, *J* = 8.0 Hz, 2H), 2.78 (dq, *J* = 32.2, 7.5 Hz, 4H), 1.36 (d, *J* = 2.4 Hz, 24H). MS (ESI) m/z: 796.42, found 797.43 $[M + H]^+$.

Compound 3 (5.0 g, 6.20 mmol) was dissolved in 50 mL MeOH with NaOH (2 g, 50 mmol) under ice bath conditions. The reaction mixture was stirred at room temperature for 6 h. After completion of the reaction, the pH was adjusted to pH = 2-3 with citric acid solution (pH = 2). The solvent was removed under reduced pressure. The residue was diluted with ethyl acetate and washed with saturated NaCl (aq). The organic layer was dried over anhydrous Na_2SO_4, filtered, and concentrated under reduced pressure to obtain Compound 4 (yield: 90%).

^{1}H NMR (400 MHz, DMSO) δ 8.72 (s, 1H), 8.25 (s, 1H), 8.02 (d, *J* = 8.3 Hz, 1H), 7.46 (d, *J* = 6.5 Hz, 9H), 7.14 (dd, *J* = 7.3, 2.5 Hz, 6H), 7.08 (s, 1H), 6.94 (t, *J* = 5.7 Hz, 1H), 6.75 (t, *J* = 5.8 Hz, 1H), 4.71 (s, 1H), 4.13 (td, *J* = 8.2, 5.2 Hz, 1H), 3.52 (d, *J* = 5.7 Hz, 2H), 3.07 (d, *J* = 14.8 Hz, 1H), 2.85 (dd, *J* = 16.6, 8.5 Hz, 3H), 1.35 (s, 24H). MS (ESI) m/z: 782.40, found 783.42 $[M + H]^+$.

Compound 4 (1.94 g, 2.47 mmol), H-Lys-OMe·2HCl (0.24 g, 1.03 mmol), PYBOP (1.62 g, 3.10 mmol) and HOBT (0.42 g, 3.10 mmol) were dissolved in DMF (40 mL) under nitrogen atmosphere and ice bath conditions. DIPEA (1.08 mL, 6.20 mmol) was slowly added into the mixture. The reaction mixture was stirred at room temperature for 24 h. After completion of the reaction, the solvent was removed under reduced pressure, and the residue was dissolved in ethyl acetate. The organic phase was washed three times sequentially with saturated $NaHCO_3$ (aq), 0.1 M HCl, and saturated NaCl (aq), respectively. The organic layer was dried over anhydrous Na_2SO_4, filtered, and concentrated under reduced pressure. Compound 5 was isolated by silica gel column chromatography using a dichloromethane/methanol (DCM:MeOH = 20:1, V/V) eluent (yield: 61%).

^{1}H NMR (500 MHz, DMSO) δ 7.95 (t, *J* = 38.4 Hz, 5H), 7.41 (p, *J* = 5.1, 3.9 Hz, 18H), 7.23 (d, *J* = 7.4 Hz, 2H), 7.09 (d, *J* = 7.4 Hz, 12H), 6.96 (d, *J* = 19.0 Hz, 2H), 6.70 (q, *J* = 9.2, 8.1 Hz, 4H), 4.56 (d, *J* = 54.2 Hz, 2H), 4.18 (d, *J* = 69.9 Hz, 3H), 3.56 (tt, *J* = 18.3, 9.3 Hz, 7H), 3.03 – 2.77 (m, 10H), 1.66 – 1.20 (m, 54H). MS (MALDI) m/z: 1688.90, found 1712.35 $[M + Na]^+$.

Compound 5 (1 g, 0.59 mmol) was dissolved in DCM (2.6 mL) under nitrogen atmosphere and ice bath conditions. Trifluoroacetic acid (2.6 mL, 35.53 mmol) was slowly added into the mixture. The reaction mixture was stirred at room temperature for 6 h. After completion of the reaction, the solvent was removed under reduced pressure. The organic layer was dried over anhydrous Na_2SO_4, filtered, and concentrated under reduced pressure to obtain Compound 6 (yield: 85%).

^{1}H NMR (400 MHz, DMSO) δ 8.96 (s, 2H), 8.83 – 8.63 (m, 2H), 8.44 (dd, *J* = 23.9, 7.0 Hz, 1H), 8.36 – 8.24 (m, 2H), 8.02 (s, 4H), 7.82 (s, 3H), 7.39 – 7.28 (m, 2H), 4.76 (tt, *J* = 16.1, 8.0 Hz, 2H), 4.37 – 4.24 (m, 1H), 4.15 (d, *J* = 9.7 Hz, 2H), 3.38 (q, *J* = 7.0 Hz, 4H), 3.13 – 2.87 (m, 6H), 2.74 (s, 4H), 1.75 – 1.13 (m, 18H), 1.09 (t, *J* = 7.0 Hz, 5H). MS (ESI) m/z:804.47, found 403.25 $[M/2 + H]^+$.

Compound 6 (0.80 g, 0.99 mmol) was dissolved in 20 mL MeOH with NaOH (0.80 g, 20 mmol) under ice bath conditions. The reaction mixture was stirred at room temperature for 6 h. After completion of the reaction, the pH was adjusted to pH = 5-6 with hydrochloric acid solution (pH = 2). The solvent was removed under reduced pressure. The residue was diluted with ethyl acetate (100 mL) and deionized water (200 mL). The mixture was then sonicated to form a suspension, centrifuged, and the supernatant was collected and concentrated to

10 mL. The concentrated solution was dialyzed with deionized water for 72 h, and then lyophilized to obtain D-P (yield: 90%).

^{1}H NMR (400 MHz, D_2O) δ 7.78 (s, 2H), 7.01 (s, 2H), 4.71 – 4.60 (m, 2H), 4.44 – 4.03 (m, 3H), 3.80 – 3.74 (m, 4H), 3.32 – 2.88 (m, 10H), 1.85 – 1.11 (m, 18H)[13].C NMR (151 MHz, D_2O) δ 178.88, 172.79, 172.16, 172.10, 167.38, 167.21, 134.76, 134.56, 129.96, 129.66, 117.45, 54.20, 54.17, 53.68, 53.46, 53.08, 40.64, 40.59, 39.33, 39.28, 37.38, 30.79, 30.39, 30.37, 28.05, 27.65, 27.48, 27.40, 22.63, 22.18, 22.04. HRMS (m/z): $[M]^+$ calcd. for $C_{34}H_{58}N_{14}O_8$, 790.456; found, 790.4546; analysis (calcd., found for $C_{34}H_{58}N_{14}O_8$): C (51.63, 51.62), H (7.39, 7.40), O (16.18,16.19), N (24.79, 24.80).

Synthesis of (((ethane-1,2-diylbis(azanediyl))bis(carbonyl)) bis(4,1-phenylene))diboronic acid(EBPBA)

4-Carboxyphenylboronic acid (3.65 g, 22.00 mmol), ethylenediamine dihydrochloride (1.33 g, 10.00 mmol), HATU (11.40 g, 30.00 mmol) and HOAT (4.08 g, 30.00 mmol) were dissolved in DMF (40 mL) under nitrogen atmosphere and ice bath conditions. DIPEA (10.45 mL, 60.00 mmol) was slowly added to the mixture. The reaction mixture was stirred at room temperature for 12 h. After completion of the reaction, the solvent was removed under reduced pressure. The mixture was diluted with deionized water (200 mL) and filtered. The solid product was collected and dried under vacuum to obtain EBPBA.

^{1}H NMR (300 MHz, DMSO) δ 8.63 (d, J = 5.2 Hz, 2H), 8.09 (d, J = 72.6 Hz, 4H), 7.83 (q, J = 8.2 Hz, 8H), 3.44 (d, J = 4.5 Hz, 4H). MS (ESI) m/z:356.14, found 379.13 $[M + Na]^+$.

Preparation and characterization of D-CuP

24 mM D-P solution and 24 mM $CuSO_4$ solution were mixed in equal volumes (the D-P: Cu^{2+} ratio was 1:0.5) and stirred overnight at room temperature to obtain 12 mM D-CuP solution. The absorption spectrum of 12 mM D-P, D-CuP, $CuSO_4$, and 24 mM M-CuP aqueous solutions was obtained using a UV−Vis spectrophotometer (MAPADA, UV-1800PC). Electron paramagnetic resonance (EPR) spectroscopy was conducted using a Bruker A300-10/12 to verify the successful coordination of Cu^{2+} with D-P.

pH stability of M-CuP and D-CuP

24 mM D-CuP and 12 mM M-CuP aqueous solutions (1 mL) were separately incubated with 1 mL of PBS at varying pH values (pH 4 to 9) at 37 °C for 24 h. To simulate extreme acidic conditions, PBS (pH=1) was used as the positive control group (PC). The absorbance of D-CuP and M-CuP solutions at 584 nm was measured using a UV−Vis spectrophotometer.

In vitro biostability of M-CuP and D-CuP against Proteinase K

1 mM D-CuP and 2 mM M-CuP aqueous solutions (1 mL) were incubated separately with Proteinase K (10 U mL^{-1}, 100 μL) at 37 °C for 0, 1, 2 and 4 h. Methanol (400 μL) was then added to stop the reaction. The samples were centrifuged at 13000 g for 10 min at 4 °C and the supernatant was collected and detected by HPLC to analyze the biostability of M-CuP and D-CuP against proteinase K.

Preparation of G/D-CuP

15% PVA-1788 (w/w) solution (1 mL), 12 mM D-CuP solution (650 μL), and EBPBA solution (5 mg mL^{-1}, 350 μL) were mixed thoroughly and stirred rapidly to obtain G/D-CuP.

Rheological properties and characterization of G/D-CuP

The rheological properties of G/D-CuP were evaluated using a rheometer (TA Instruments, DHR-2). The strain sweep was conducted at a constant angular frequency of 3.14 rad s^{-1} and a strain range of 0.1% to 1200%. Frequency sweep measurements were performed at 5% strain and a frequency range of 500 to 0.1 rad s^{-1}. To assess self-healing behavior, a continuous step-strain test was conducted by alternating between low strain (1%, 65 s) and high strain (1200%, 65 s) for three cycles. The morphologies of lyophilized hydrogels were examined by scanning electron microscopy (SEM, Hitachi S-3400N) at an accelerating voltage of 5 kV. The surface of lyophilized hydrogel was sprayed with platinum to increase the electrical conductivity.

D-CuP release from G/D-CuP

G/D-CuP was loaded into a dialysis bag (MWCO = 3.5 kDa) and immersed in PBS (pH 7.4) without or with 1 mM H_2O_2. The samples were placed in a shaker at 37 °C and shaken at 80 rpm. The release medium was collected at predetermined time points and replenished with fresh medium. The D-CuP release efficiency was measured by UV-vis spectrophotometer at 600 nm.

Cell lines

Human endothelial cells HUVEC (CC-Y1285) were purchased from EK-Bioscience (Shanghai, China). Mouse fibroblast cells NIH/3T3 (SCSP-515), mouse fibroblast cells L-929 (SCSP-5039) and mouse macrophage cells RAW 264.7 (SCSP-5036) were purchased from Chinese Academy of Science Cell Bank for Type Culture Collection (Shanghai, China). The cells were maintained in an incubator at 37 °C, with above 95% humidity and 5% CO_2.

The cellular uptake of D-CuP

NIH/3T3 cells were plated in a 24-well plate (5×10^4 cells per well) and cultured for 24 h. The cells were incubated with free FITC-D-CuP or FITC-M-CuP (identical in GHK and FITC molar concentrations) for 6 h. The nuclei were stained with Hoechst 33342. Fluorescence signals were visualized using a fluorescence microscope (Nikon Ts2R) and quantified by flow cytometry (NovoCyte 3000, Agilent, USA).

In vitro macrophage phenotype regulation of G/D-CuP

RAW264.7 cells were seeded on confocal culture dishes (1×10^5 cells per well) and cultured for 24 h. For M1 polarization, RAW264.7 cells were stimulated with LPS (100 ng mL^{-1}, Sigma-Aldrich, USA) and IFN-γ (20 ng mL^{-1}, ABclonal, China) for 24 h. The culture medium was then replaced with 30 μM M-CuP solution, 15 μM D-CuP solution, or hydrogel extract at 37 °C for another 24 h. For M2 polarization, RAW264.7 cells were stimulated with IL-4 (20 ng mL^{-1}, ABclonal, China) for 24 h. Immunofluorescent staining was performed to analyze the expression of M2 gene markers. RAW264.7 cells were fixed with 4% paraformaldehyde, permeabilized with ice-cold methanol, and blocked with MinuteBlock Blocking Buffer (Affinibody, China). Cells were incubated with rabbit polyclonal antibody against CD206 (1:500, Cat No. WL06177, Lot No. T05076177, Wanleibio, China), followed by CoraLite594 goat anti-Rabbit IgG(H + L) secondary antibody (1:500, Cat No. SA00013-4, Lot No. 20000842, Proteintech, China). The nuclei of macrophages were stained with DAPI. Fluorescence was detected by confocal laser scanning microscopy (CLSM) (Zeiss, LSM800, Germany).

To quantify the proportion of M2 macrophages, cells were stained with APC anti-mouse CD206 antibodies (BioLegend, USA) and PE-Cy7 anti-mouse CD86 antibodies (BD, Cat No. 560582, Lot No. 0009083, USA) for 30 min at 4 °C. Data were obtained by flow cytometry (NovoCyte3000, Agilent, USA) and analyzed using FlowJo V10 software.

Elisa

RAW264.7 cells (3×10^5 cells per well) pre-treated with LPS (1 μg mL^{-1}) for 24 h and untreated HUVECs (3×10^5 cells per well) were incubated with different materials for 24 h. The supernatants were collected and the amount of TNF-α, IL-6, and VEGF secreted were measured by ELISA kits (KeyGEN, China).

ROS scavenging ability of G/D-CuP

Fenton reaction was used to determine the efficiency of G/D-CuP to scavenge hydroxyl radical. Specifically, 2 mM $FeSO_4$ solution, 360 mg mL^{-1} safranine solution, 3% (wt%) H_2O_2 solution, 0.1 M HCl (aq) and G/D-CuP were added to each well in a 96-well plate (n = 3). The negative control group (NC) did not contain G/D-CuP. The blank control group (BC) did not contain H_2O_2 solution and G/D-CuP. The mixture was incubated at 55 °C for 1 h. After the mixture cooled down, the absorbance value at 500 nm was measured using a microplate reader. H_2O_2 scavenging ratio (%) = $(A - A_n)/(A_b - A_n) \times 100\%$, where A represents the absorbance value for the sample group, A_b represents the absorbance value for the BC group and A_n is the absorbance value for the NC group. The ability of G/D-CuP to scavenge ROS was evaluated using a ROS fluorescent probe (DCFH-DA).

NIH/3T3 cells were seeded on 6-well plates (2×10^4 cells per well) and cultured for 24 h. The cell was treated with a medium that included 500 μM H_2O_2 solution that was treated with a variety of materials. The negative control group (NC) did not contain materials and the blank control group (BC) did not contain H_2O_2 solution and materials. After incubation for 1 h, the DCFH-DA probe (10 μM) was added and incubated in the dark for 30 min to detect ROS. Hoechst 33342 (4 μg mL^{-1}) was then added and incubated at 37 °C for 5 min to stain the cell nuclei. The fluorescence was detected by fluorescence microscope (Nikon, Ts2R) and flow cytometry (BD, FACSCelesta).

Cellular SOD activity assay

NIH/3T3 cells were seeded on 6-well plates (2×10^5 cells per well) and cultured for 24 h. The cells were treated with a medium that included 500 μM H_2O_2 solution that was treated with a variety of materials. The negative control group (NC) did not contain materials and the blank control group (BC) did not contain H_2O_2 solution and materials. After incubation for 24 h, the cellular SOD activity was measured by a Total Superoxide Dismutase Assay Kit with WST-8 (Beyotime, China).

Hemolysis assay

The various concentrations of D-CuP solution or hydrogel extract (G or G/D-CuP) (500 μL) and 2% (v/v) red blood cells (RBC) suspension (500 μL) were added to a 1.5 mL tube as sample groups. Ultrapure water was used as the positive control group (PC), and the physiological saline was used as the negative control group (NC). After incubating at 37 °C for 2 h, the samples were centrifuged at 360 g for 10 min, and then each sample (200 μL) was transferred to a 96-well plate. The absorbance value at 540 nm was measured using a microplate reader. Hemolysis ratio (%) = $(A - A_n)/(A_p - A_n) \times 100\%$, where A represents the absorbance value for the sample group, A_p represents the absorbance value for the positive group and A_n is the absorbance value for the negative group.

MTT assay

NIH/3T3 cells were seeded on 96-well plates (5×10^3 cells per well) and cultured for 24 h. The culture medium was replaced with various concentrations of G extract, D-CuP solution, G/D-CuP extract and blank medium (blank control group, BC) (100 μL) (n = 4). After further culturing for 24 h, each well was washed, 1 mg mL^{-1} MTT solution (100 μL) was added, and the cells were re-incubated for 4 h in the dark. The MTT solution was removed and DMSO (150 μL) was added to dissolve formazan. Finally, the optical density at 490 nm (OD490) was measured using a microplate reader (MD, SpectraMax M2e).

Co-culture of cells with G/D-CuP

G/D-CuP was prepared in a confocal dish. NIH/3T3 cells (5×10^4 cells per well) were seeded onto the hydrogel surface and incubated for 24 h. NIH/3T3 cells were stained with 0.5 μM Calcein-AM and the fluorescence was detected by CLSM.

Ki-67 immunofluorescence staining

HUVEC cells were seeded on confocal culture dishes (1×10^5 cells per well) and incubated with different materials for 24 h. HUVEC cells were fixed with 4% paraformaldehyde, permeabilized with ice-cold methanol and blocked with MinuteBlock Blocking Buffer (Affinibody, China). Cells were incubated with rabbit polyclonal antibody against Ki67 (1:500, Cat No. 28074-1-AP, Lot No. 00141310, Proteintech, China), followed by CoraLite488 goat anti-Rabbit IgG(H + L) secondary antibody (1:500, Cat No. SA00013-2, Lot No. 20000839, Proteintech, China). The nuclei of macrophages were stained with DAPI. Fluorescence was detected by CLSM.

Tube formation assay

Angiogenesis was assessed by tube formation assay. High concentration Matrigel 10 μL (40187, Yeasen, China) was added into μ-Slide Angiogenesis per well and polymerized at 37 °C for 2 h. HUVEC cells were seeded onto the Matrigel (1×10^4 cells per well) and incubated with different materials for 24 h. HUVEC cells were stained with 0.5 μM Calcein-AM and the fluorescence was detected by fluorescence microscope, and quantitative analysis of each image was performed using Image J 1.53t software.

Transwell migration assay

L929 cells (1×10^5 cells per well) were seeded into the upper chamber (8 μm pore size). The lower chamber was added with various materials supplemented with 10% FBS, while serum-free DMEM was added to the upper chamber. After 24 h, migrated cells on the upper surface of the filter were removed with a cotton swab, while the cells on the bottom of the filter were fixed with 4% paraformaldehyde at room temperature for 15 min and stained with 3% crystal violet solution for 15 min. The migrated cells were detected by a light microscope, and quantitative analysis of each image was performed using Image J software.

Cell scratch experiment

L929 cells were seeded in 6-well plates (8×10^5 cells per well) and cultured for 24 h to form a cell monolayer. Subsequently, the cell monolayer was scratched using a 200 μL pipette and then washed twice with PBS. The cells were incubated with the 30 μM M-CuP or 15 μM D-CuP solution (2 mL). Cell images were captured at 0, 8, 18, and 30 h by fluorescence microscope. Scratch healing rate (%) = $(C_0 - C_t)/C_0 \times 100\%$, where C_0 represents the scratch area at 0 h and C_t represents the scratch area at specific times. The scratch areas were measured using Image J software.

Proteomics analysis

Label-free LC-MS/MS was used for proteomics analysis of the blank group and D-CuP group (n = 3 in each group). After protein extraction, Filter-Aided Sample Preparation (FASP) was used for digestion. Orbitrap-Fusion mass spectrometer (Thermo Finnigan, San Jose, CA) was used for mass spectrometry analysis. Proteome Discoverer 2.4 software (Thermo Scientific) with the built-in Sequest algorithm was used for database searching and quantitative analysis. P-value < 0.05 and a fold change ratio >1.2 were considered as significantly differentially expressed proteins (DEPs).

Molecular docking

The protein structures of p53 (PDB ID: 8E7A) and HDAC7 (PDB ID: 3C0Y) were obtained from the Protein Data Bank (https://www.rcsb.org). Ligands and receptor proteins were preprocessed using AutoDock Tools 1.5.6, and molecular docking was performed using AutoDock Vina. Structural visualization, image processing, and analysis of docking results were performed using PyMOL 2.5.2.

Surface plasmon resonance (SPR) analysis

SPR measurements were performed using a WeSPR™ OneAuto instrument (XLEMENT) maintained at 25 °C. Recombinant human p53 (Proteintech, Cat. No. AG0698) or HDAC7 (Proteintech, Cat. No. AG24396) was immobilized onto carboxyl sensor chips. Analytes (M-CuP or D-CuP) were diluted in PBST buffer (10 mM phosphate-buffered saline, 0.05% Tween-20, pH 7.4) and injected at increasing concentrations at a flow rate of 30 µL/min, with 120 s association and 180 s dissociation phases. The running buffer (PBST, 25 °C) was degassed prior to use. Sensorgrams were analyzed using a global fit to the 1:1 Langmuir binding model.

Animal study

The C57BL/6 mice (male, 5–6 weeks old) were purchased from SPF (Beijing) Biotechnology Co., Ltd. All animals were bred in the pathogen-free facility with a 12 h light/dark cycle at temperature (20–25 °C), relative humidity (40–60%), and had ad libitum access to food and water.

In vivo retention of G/D-CuP and release of D-CuP

To assess the spatiotemporal retention of G/D-CuP, it was topically applied to full-thickness dorsal wounds in diabetic mice. Dynamic imaging was performed at 0, 2, 12, 16, 20, 32, and 48 h post-application to monitor hydrogel distribution. The G/D-CuP denoted the unlabeled hydrogel, while the CV-G/D-CuP represented the hydrogel labeled with Crystal Violet dye for enhanced visual observation.

FITC-conjugated D-CuP hydrogel was uniformly applied to the dorsal wounds in darkness. Hydrogel residues were collected at specified time points, and their weight was recorded to determine the weight loss. To analyze drug release, the collected hydrogels were dissolved in deionized water, vortexed, and centrifuged. The fluorescence intensity of the supernatant was subsequently measured.

In vivo diabetic wound healing of G/D-CuP

Male C57BL/6 mice were fed with a high-sugar, high-fat diet for four weeks, followed by intraperitoneal injection of premade streptozotocin (STZ) solution at a dose of 50 mg kg^{-1} daily for one week. Mice exhibiting fasting blood glucose levels above 16.7 mmol L^{-1} were considered as successfully established and were subsequently randomly assigned into six groups (n = 6): PBS (Blank control group), G, M-CuP solution, D-CuP solution, G/M-CuP and G/D-CuP. Mice without injected STZ were set as a Negative control group. A full-thickness skin wound with a diameter of 6 mm was created on the dorsal region of each mouse. On days 3, 7, and 12 post-treatment, wound images were captured using a fixed camera setup that included a scale bar within the field of view. Wound areas were quantified using ImageJ software, and all measurements were normalized to the scale bar.

Expression of cytokines and growth factors

Wound skin tissue samples were collected from sacrificed mice on the 3rd day and immersed in normal saline, mechanically broken into tissue homogenate, and the supernatants were collected. Protein levels of IL-6, IL-10, and VEGF were quantified using ELISA kits and normalized to total protein content measured by the BCA Protein Assay Kit. Normalized expression (pg mg^{-1}) = Cytokine concentration (pg mL^{-1})/ Total protein concentration (mg mL^{-1}).

Histological analysis

Regenerated skin samples were excised and collected on the 7th and 12th day from sacrificed mice. Skin samples were fixed with 4% paraformaldehyde, embedded in paraffin, and sectioned for H&E, Masson, and immunohistochemical staining. Immunohistochemical staining was performed for TNF-α, IL-6, and IL-10 to evaluate the inflammatory response in the tissue, VEGF and CD31 to evaluate angiogenesis, and Ki67 to assess cell proliferation. Immunofluorescence staining was conducted to assess antioxidant capacity via SOD expression and to evaluate macrophage polarization using CD86 (M1 marker) and CD206 (M2 marker). The slide images were captured by an inverted microscope and the average optical density (AOD) was measured using Image J 1.53t software.

Statistics and reproducibility

For assessing differences between the two groups, a t-test was performed. Differences among more than two groups were analyzed using one-way ANOVA or two-way ANOVA with GraphPad Prism 9.0 software (GraphPad Software, Inc.; San Diego, CA). Data are expressed as Mean ± SD, n = 3 independent replicates. In each group, any $p < 0.05$ was considered statistically significant. NS represents no significant difference. Results from representative experiments (such as micrographs) were obtained from at least three independent fields of view with similar results. The enrich plots were drawn using ChiPlot (https://www.chiplot.online/).

Data availability

All the proteome datasets for the cohort study can be accessed through the ProteomeXchange ID: PXD059903. The source data generated in this study are provided in the Supplementary Information/ Source Data file. Source data is available for Figs. 2–8 and Supplementary Figs. 5, 11–16, 18, 23, 25, 26 in the associated source data file. The authors declare that all data supporting the findings of this study are available within the article and the Supplementary Information. All other data are available from the corresponding authors upon request. Source data are provided with this paper.

References

1. Chung, I., Akita, R., Vandlen, R., Toomre, D., Schlessinger, J. & Mellman, I. Spatial control of EGF receptor activation by reversible dimerization on living cells. *Nature* **464**, 783–U163 (2010).
2. Zhang, H. et al. Dimerization and antidepressant recognition at noradrenaline transporter. *Nature* **630**, 247–254 (2024).
3. Kim, T. H. et al. The role of dimer asymmetry and protomer dynamics in enzyme catalysis. *Science* **355**, eaag2355 (2017).
4. Seavill, P. W. Dimers or polymers. *Nat. Synth.* **1**, 410–410 (2022).
5. Shen, C. et al. Structural basis of GABAB receptor–Gi protein coupling. *Nature* **594**, 594–598 (2021).
6. Bertschi, A., Wang, P. L., Galvan, S., Teixeira, A. P. & Fussenegger, M. Combinatorial protein dimerization enables precise multi-input synthetic computations. *Nat. Chem. Biol.* **19**, 767 (2023).
7. Li, Y. J. et al. Structural basis for activity regulation of MLL family methyltransferases. *Nature* **530**, 447 (2016).
8. Wonganu, B. & Berger, B. W. A specific, transmembrane interface regulates fibroblast activation protein (FAP) homodimerization, trafficking and exopeptidase activity. *Biochim. Biophys. Acta Biomembr.***1858**, 1876–1882 (2016).
9. Marianayagam, N. J., Sunde, M. & Matthews, J. M. The power of two: protein dimerization in biology. *Trends Biochem. Sci.* **29**, 618–625 (2004).
10. Dang, D. T. Molecular approaches to protein dimerization: opportunities for supramolecular chemistry. *Front. Chem.* **10**, 829312 (2022).
11. Sun, J. W., Yang, H. & Tang, W. J. Recent advances in total syntheses of complex dimeric natural products. *Chem. Soc. Rev.* **50**, 2320–2336 (2021).
12. Manigrasso, J. et al. Author Correction: Visualizing group II intron dynamics between the first and second steps of splicing. *Nat. Commun.* **13**, 1 (2022).
13. Kim, M., Jo, H., Jung, G. Y. & Oh, S. S. Molecular complementarity of proteomimetic materials for target-specific recognition and recognition-mediated complex functions. *Adv. Mater.* **35**, 2208309 (2023).

14. Paquin, A., Reyes-Moreno, C. & Bérubé, G. Recent advances in the use of the dimerization strategy as a means to increase the biological potential of natural or synthetic molecules. *Molecules* **26**, 2340 (2021).
15. Waldhoer, M. et al. A heterodimer-selective agonist shows relevance of G protein-coupled receptor dimers. *Proc. Natl. Acad. Sci. USA* **102**, 9050–9055 (2005).
16. Hiller, C., Kühhorn, J. & Gmeiner, P. Class A G-protein-coupled receptor (GPCR) dimers and bivalent ligands. *J. Med. Chem.* **56**, 6542–6559 (2013).
17. Theocharidis, G. et al. A strain-programmed patch for the healing of diabetic wounds. *Nat. Biomed. Eng.* **6**, 1118 (2022).
18. Matoori, S., Veves, A. & Mooney, D. J. Advanced bandages for diabetic wound healing. *Sci. Transl. Med.* **13**, eabe4839 (2021).
19. McDermott, K., Fang, M., Boulton, A. J. M., Selvin, E. & Hicks, C. W. Etiology, epidemiology, and disparities in the burden of diabetic foot ulcers. *Diabetes Care* **46**, 209–221 (2023).
20. Chen, L., Sun, S., Gao, Y. & Ran, X. Global mortality of diabetic foot ulcer: a systematic review and meta-analysis of observational studies. *Diabetes Obes. Metab.* **25**, 36–45 (2022).
21. Xia, H. et al. Glycopeptide-based multifunctional hydrogels promote diabetic wound healing through pH regulation of microenvironment. *Adv. Funct. Mater.* **33**, 2215116 (2023).
22. Wang, X. et al. Early controlled release of peroxisome proliferator-activated receptor β/δ agonist GW501516 improves diabetic wound healing through redox modulation of wound microenvironment. *J. Control Release* **197**, 138–147 (2015).
23. Xin, P. K. et al. Natural okra-based hydrogel for chronic diabetic wound healing. *Chin. Chem. Lett.* **34**, 108125 (2023).
24. Luo, M. et al. Solid-state atomic hydrogen as a broad-spectrum RONS scavenger for accelerated diabetic wound healing. *Natl. Sci. Rev.* **11**, nwad269 (2024).
25. Chen, Y. et al. Research advances in smart responsive-hydrogel dressings with potential clinical diabetic wound healing properties. *Mil. Med. Res.* **10**, 37 (2023).
26. He, L. N. et al. Photothermal antibacterial materials to promote wound healing. *J. Control Release* **363**, 180–200 (2023).
27. Puthia, M. et al. A dual-action peptide-containing hydrogel targets wound infection and inflammation. *Sci. Transl. Med.* **12**, eaax6601 (2020).
28. Powell, L. C. et al. Topical, immunomodulatory epoxy-tiglianes induce biofilm disruption and healing in acute and chronic skin wounds. *Sci. Transl. Med.* **14**, eabn3758 (2022).
29. Dong, R. N. & Guo, B. L. Smart wound dressings for wound healing. *Nano Today* **41**, 101290 (2021).
30. Xu, J. Q., Zhu, X. G., Zhao, J. H., Ling, G. X. & Zhang, P. Biomedical applications of supramolecular hydrogels with enhanced mechanical properties. *Adv. Colloid Interface Sci.* **321**, 103000 (2023).
31. Guan, T., Li, J. Y., Chen, C. Y. & Liu, Y. Self-assembling peptide-based hydrogels for wound tissue repair. *Adv. Sci.* **9**, 2104165 (2022).
32. Teng, R. X. et al. In situ enzyme-induced self-assembly of antimicrobial-antioxidative peptides to promote wound healing. *Adv. Funct. Mater.* **33**, 2214454 (2023).
33. Pickart, L., Vasquez-Soltero, J. M. & Margolina, A. GHK peptide as a natural modulator of multiple cellular pathways in skin regeneration. *Biomed. Res. Int.* **2015**, 648108 (2015).
34. Li, Y. et al. Bio-inspired supramolecular metallopeptide hydrogel promotes recovery from cutaneous wound. *Chem. Eng. J.* **455**, 140848 (2023).
35. Lee, S. et al. In situ photo-crosslinkable hyaluronic acid-based hydrogel embedded with GHK peptide nanofibers for bioactive wound healing. *Acta Biomater.* **172**, 159–174 (2023).
36. Wang, Y. et al. GHK-Cu/Pionin-loaded in situ electrospun PVB/PVP smart dressing promotes wound healing via anti-oxidant, anti-inflammatory, antimicrobial, and tissue regenerative effects. *Chem. Eng. J.* **492**, 152154 (2024).
37. Liu, T. Q. et al. Thermodynamically stable ionic liquid microemulsions pioneer pathways for topical delivery and peptide application. *Bioact. Mater.* **32**, 502–513 (2024).
38. Ouberai, M. M. et al. Controlling the bioactivity of a peptide hormone in vivo by reversible self-assembly. *Nat. Commun.* **8**, 1026 (2017).
39. Tan, P., Tang, Q., Xu, S. R., Zhang, Y. C., Fu, H. Y. & Ma, X. Designing self-assembling chimeric peptide nanoparticles with high stability for combating piglet bacterial infections. *Adv. Sci.* **9**, 2105955 (2022).
40. Jing, X. & Jin, K. A gold mine for drug discovery: strategies to develop cyclic peptides into therapies. *Med. Res. Rev.* **40**, 753–810 (2020).
41. Qian, Z. Q. et al. Enhancing the cell permeability and metabolic stability of peptidyl drugs by reversible bicyclization. *Angew. Chem. Int. Ed.* **56**, 1525–1529 (2017).
42. Xu, L. et al. Spontaneously restoring specific bioaffinity of RGD in linear RGD-containing peptides by conjugation with zwitterionic dendrimers. *Acta Biomater.* **148**, 61–72 (2022).
43. Li, Y. et al. Multi-lasso peptide-based synergistic nanocomposite: a high-stability, broad-spectrum antimicrobial agent with potential for combined antibacterial therapy. *ACS Nano* **18**, 31435–31450 (2024).
44. Zeng, Z. et al. Customized reversible stapling for selective delivery of bioactive peptides. *J. Am. Chem. Soc.* **144**, 23614–23621 (2022).
45. Imura, Y., Nishida, M., Ogawa, Y., Takakura, Y. & Matsuzaki, K. Action mechanism of tachyplesin I and effects of PEGylation. *Biochim. Biophys. Acta Biomembr.* **1768**, 1160–1169 (2007).
46. Wang, X. et al. Liposomes with cyclic RGD peptide motif triggers acute immune response in mice. *J. Control. Release* **293**, 201–214 (2019).
47. Thell, K., Hellinger, R., Schabbauer, G. & Gruber, C. W. Immunosuppressive peptides and their therapeutic applications. *Drug Discov. Today* **19**, 645–653 (2014).
48. Pollard, J. D., Quan, S., Kang, T. & Koch, R. J. Effects of copper tripeptide on the growth and expression of growth factors by normal and irradiated fibroblasts. *Arch. Facial Plast. Surg.* **7**, 27–31 (2005).
49. Galanakou, C., Dhumal, D. & Peng, L. Amphiphilic dendrimers against antibiotic resistance: light at the end of the tunnel?. *Biomater. Sci.* **11**, 3379–3393 (2023).
50. Wang, J. et al. Antimicrobial peptides with high proteolytic resistance for combating gram-negative bacteria. *J. Med. Chem.* **62**, 2286–2304 (2019).
51. Lei, L. et al. Dual-functional injectable hydrogel for osteoarthritis treatments. *Adv. Healthc. Mater.* **13**, 2302551 (2023).
52. Li, H., Li, B., Lv, D., Li, W., Lu, Y. & Luo, G. Biomaterials releasing drug responsively to promote wound healing via regulation of pathological microenvironment. *Adv. Drug Del. Rev.* **196**, 114778 (2023).
53. Min, Y. et al. The pH-sensitive optical fiber integrated CMCS-PA@Fe hydrogels for photothermal therapy and real-time monitoring of infected wounds. *Adv. Funct. Mater.* **33**, 2212803 (2023).
54. Xiao, J., Zhou, Z., Zhong, G., Xu, T. & Zhang, X. Self-sterilizing microneedle sensing patches for machine learning-enabled wound pH visual monitoring. *Adv. Funct. Mater.* **34**, 2315067 (2024).
55. Chen, L., Zhao, N. J., McClements, D. J., Hamaker, B. R. & Miao, M. Advanced dendritic glucan-derived biomaterials: from molecular structure to versatile applications. *Compr. Rev. Food Sci. Food Saf.* **22**, 4107–4146 (2023).
56. Shu, X. et al. ROS-scavenging hydrogel to accelerate wound healing and reduce scar formation. *Chem. Eng. J.* **474**, 145941 (2023).

57. Qu, M. Y. et al. An ROS-scavenging treg-recruiting hydrogel patch for diabetic wound healing. *Adv. Funct. Mater.* **34**, 2314500 (2024).
58. Qiao, L. et al. Antibacterial conductive self-healing hydrogel wound dressing with dual dynamic bonds promotes infected wound healing. *Bioact. Mater.* **30**, 129–141 (2023).
59. Wen, N. et al. Bio-inspired self-healing hydrogel for fast hemostasis and accelerated wound healing of gastric ulcers. *Adv. Funct. Mater.* **35**, 2411959 (2024).
60. Teng, L. et al. Biomimetic glycopolypeptide hydrogels with tunable adhesion and microporous structure for fast hemostasis and highly efficient wound healing. *Adv. Funct. Mater.* **31**, 2105628 (2021).
61. Wang, S. et al. Triple cross-linked dynamic responsive hydrogel loaded with selenium nanoparticles for modulating the inflammatory microenvironment via PI3K/Akt/NF-κB and MAPK signaling pathways. *Adv. Sci.* **10**, 2303167 (2023).
62. Zhou, X. Y. et al. Dual glucose/ROS-sensitive injectable adhesive self-healing hydrogel with photothermal antibacterial activity and modulation of macrophage polarization for infected diabetic wound healing. *ACS Mater. Lett.* **5**, 3142–3155 (2023).
63. Lu, Y. F. et al. Engineering bacteria-activated multifunctionalized hydrogel for promoting diabetic wound healing. *Adv. Funct. Mater.* **31**, 2105749 (2021).
64. Guo, Y. et al. Multifunctional PtCuTe nanosheets with strong ROS scavenging and ROS-independent antibacterial properties promote diabetic wound healing. *Adv. Mater.* **36**, 2306292 (2023).
65. Fan, J.-X. et al. Engineered bacterial bioreactor for tumor therapy via Fenton-like reaction with localized H2O2 generation. *Adv. Mater.* **31**, 1808278 (2019).
66. Pickart, L. & Margolina, A. Regenerative and protective actions of the GHK-Cu peptide in the light of the new gene data. *Int. J. Mol. Sci.* **19**, 1987 (2018).
67. Shi, C. et al. Hyaluronic acid-based reactive oxygen species-responsive multifunctional injectable hydrogel platform accelerating diabetic wound healing. *Adv. Healthc. Mater.* **13**, 2302626 (2024).
68. Yang, Y. et al. Ubiquitination flow repressors: enhancing wound healing of infectious diabetic ulcers through stabilization of poly-ubiquitinated hypoxia-inducible factor-1α by theranostic nitric oxide nanogenerators. *Adv. Mater.* **33**, 2103593 (2021).
69. Wang, Y. C. et al. Adipose mesenchymal stem cell derived exosomes promote keratinocytes and fibroblasts embedded in collagen/platelet-rich plasma scaffold and accelerate wound healing. *Adv. Mater.* **35**, 2303642 (2023).
70. Liu, Z. L., Chen, H. H., Zheng, L. L., Sun, L. P. & Shi, L. Angiogenic signaling pathways and anti-angiogenic therapy for cancer. *Signal Transduct. Target. Ther.* **8**, 198 (2023).
71. Friedberg, E. C. How nucleotide excision repair protects against cancer. *Nat. Rev. Cancer* **1**, 22–33 (2001).
72. Turtoi, A. et al. The angiogenesis suppressor gene AKAP12 is under the epigenetic control of HDAC7 in endothelial cells. *Angiogenesis* **15**, 543–554 (2012).
73. Qian, Y. N. et al. Immunoregulation in diabetic wound repair with a photoenhanced glycyrrhizic acid hydrogel scaffold. *Adv. Mater.* **34**, 2200521 (2022).
74. Shen, X.-R. et al. Beneficial effects of a novel shark-skin collagen dressing for the promotion of seawater immersion wound healing. *Mil. Med. Res.* **4**, 33 (2017).
75. Keane, T. J., Horejs, C. M. & Stevens, M. M. Scarring vs. functional healing: matrix-based strategies to regulate tissue repair. *Adv. Drug Del. Rev.* **129**, 407–419 (2018).

Acknowledgements

This work was supported by the National Natural Science Foundation of China (No. 32271456 to L.J., No. 92163214 to X.J., No. 52333003 to X.J.), Basic Research Program of Jiangsu (BK20244003) and the Natural Science Foundation of Jiangsu Province (BK20202002). The authors also acknowledge Hui-Ying Wang of the Public Platform of State Key Laboratory of State Key Laboratory of Natural Medicines at China Pharmaceutical University for the use of analytical instrumentation facilities.

Author contributions

L.J., X.J., R.C. and C.D. developed the concepts and designed the experiments. R.C., C.D. and P.L. performed the experiments, measured data, and analyzed the results. Y.T., J.H., J.Z., Q.W., Y.C., J.T., X.J., and L.J. analyzed the results and wrote and revised the manuscript. J.T., X.J., and L.J. supervised the whole project. All authors discussed the results and commented on the paper.

Competing interests

The authors declare no competing interests.

Additional information

Supplementary information The online version contains supplementary material available at https://doi.org/10.1038/s41467-025-61141-1.

Correspondence and requests for materials should be addressed to Jiasheng Tu, Xiqun Jiang or Lei Jiang.

Peer review information *Nature Communications* thanks Hongli Mao, and the other, anonymous, reviewer for their contribution to the peer review of this work. A peer review file is available.